

RICE UNIVERSITY

Autofocus for Synthetic Aperture Radar

by

Ricardo A Gallardo Palacios

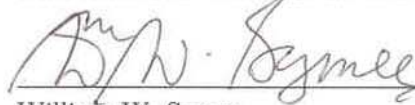
A THESIS SUBMITTED
IN PARTIAL FULFILLMENT OF THE
REQUIREMENTS FOR THE DEGREE

Master of Arts

APPROVED, THESIS COMMITTEE:



Liliana Borcea, Chair
Noah G. Harding Professor of
Computational and Applied Mathematics



William W. Symes
Noah G. Harding Professor of
Computational and Applied Mathematics



Wotao Yin
Associate Professor of Computational and
Applied Mathematics

Houston, Texas

April, 2012

ABSTRACT

Autofocus for Synthetic Aperture Radar

by

Ricardo A Gallardo Palacios

In this thesis, I compare the performance of three different autofocus techniques for Synthetic Aperture Radar (SAR). The focusing is done by estimating phase errors in SAR data. The first one, the Phase Gradient Autofocus, is the most popular in the industry, it has been around for more than 20 years and it relies on the redundancy of the phase error in the SAR images. The second one, the Entropy-based minimization, uses measurements of image sharpness to focus the images and it has been available for about 10 years. The last, the Phase-space method, uses the Wigner transform and the ambiguity function of the SAR data to estimate the phase perturbations and it was recently introduced. Additionally, I develop a criteria for filtering the data for the cases in which the Phase-space method does not capture the entirety of the error.

Acknowledgments

First, I would like to thank Dr. Liliana Borcea for all her dedication and patience in the development of this thesis. Her insight and expertise made this work possible as well as her dedication to making this manuscript understandable.

I am very grateful to the members of my committee, Dr. William Symes and Dr. Wotao Yin, for their contributions, for the discussion we have had over the years and for their willingness to help in the presentation of this work.

I am also very thankful to Dr. Thomas Callaghan, for the many many hours of discussion poured into the materialization of this thesis, his extraordinary helpfulness and providing essential algorithmic implementations that were used in this work.

I would also like to thank the wonderful staff at CAAM who have made my life easier even before I arrived to Houston.

To my family, without who's encouragement this would have never been possible, I am eternally grateful.

To all my wonderful friends in Houston, who have become a second family, I am truly thankful for your support in hours of need.

Finally, I would like to thank God, who makes it all possible and meaningful.

Contents

Abstract	ii
Acknowledgments	iii
List of Illustrations	vi
1 Synthetic Aperture Radar	1
1.1 Setup and data collection	1
1.2 Image Formation	3
1.3 Difficulties	5
1.4 Historical Developments	7
2 Autofocus	10
2.1 Phase Gradient Autofocus	11
2.1.1 Original algorithm	18
2.1.2 Examples and difficulties	19
2.2 Contrast-metric method	20
2.2.1 Entropy based autofocus	22
2.2.2 Implementation	23
2.2.3 Examples and difficulties	25
2.3 Phase-space based autofocus	28
2.3.1 Examples and difficulties	32
2.3.2 Bounds on approximation	35
2.3.3 Numerics for the filter	39
3 Numerical Comparison	41

3.1	Direct comparison	41
3.2	Effects of a adding the filter	43
3.3	Conclusions	43
A Signals		50
B Modeling of the data		53
C Gotcha		55
D Analysis for Phase-space method		56
D.1	Single target case	56
D.2	Phase estimation	57
Bibliography		59

Illustrations

1.1	SAR typical setup.	2
1.2	Perfectly focused images using one small aperture	5
1.3	Unfocused images using one small aperture.	6
2.1	Phase Gradient Autofocus Algorithm.	12
2.2	Slow time / Fast time separation	13
2.3	Phase error estimation using PGA	17
2.4	PGA example using Sandia National Laboratories SAR imagery . . .	20
2.5	Entropy based autofocus example using Sandia National Laboratories SAR imagery	26
2.6	Phase error estimation Minimizing Entropy	27
2.7	Phase-space method example using Sandia National Laboratories SAR imagery	33
2.8	Phase error estimation using the phase space method	34
2.9	Fourier transform in slow time of the data with different perturbations.	35
2.10	No single peak appears when $\ \epsilon\bar{\mu}\ / \ p_2\ \gtrsim 1$	38
2.11	Phase error estimation using the phase space method	40
3.1	Focusing by phase space method using sinusoidal noise, $\gamma = 1.33$. . .	45
3.2	Focusing by phase space method using sinusoidal noise, $\gamma = 2$	46
3.3	Focusing by phase space method using sinusoidal noise, $\gamma = 4$	47
3.4	Focusing by phase space method using sinusoidal noise, $\gamma = 8$	48

3.5	Phase-space focusing with previous filtering	49
A.1	Chirps as Linearly Frequency Modulated waveforms	52

Chapter 1

Synthetic Aperture Radar

A SAR system consist of a side looking antenna placed on the fuselage of a plane. The plane then follows a flight path over the region of interest while the antenna emits a signal at repeated times during the flight. A receiver on the plane records the signals, typically using the same antenna, known as the monostatic approach [7], that are scattered back from the targets in the imaging scene. The recordings of the scattered signals are the data.

With the acquired data, the problem of interest is to image the scene where the signals scattered. Section 1.1 describes a generic SAR system and the data processing. Section 1.2 presents the imaging process to recover the scene. Section 1.3 addresses some of the difficulties encountered in SAR and section 1.4 introduces a brief history of SAR and the existing attempts to overcome the difficulties.

1.1 Setup and data collection

The typical setup for a generic SAR system is shown in Figure 1.1. It shows a plane flying far away from the imaging scene and following a specified flightpath. The flightpath will be denoted by $\vec{\mathbf{r}}_p(s)$ and indexed by the *slow* time s . A signal is transmitted at specific slow times $s_n = n\Delta s$, $n = 0, 1, \dots$ and the time between

subsequent signal transmissions is parametrized by the *fast* time $t \in (0, \Delta s)$.

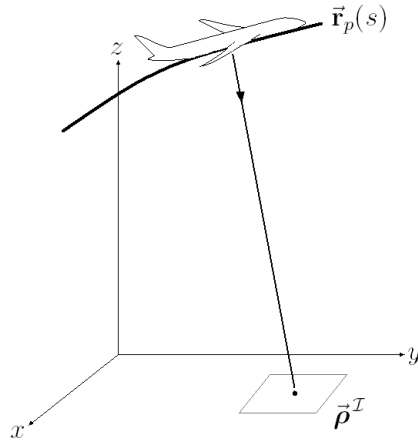


Figure 1.1 : SAR typical setup.

The collected data shall be denoted by $D(s, t)$ and it is indexed by the fast and slow times. For a model of the data see Appendix B. It is relevant to point out that any equipment records signals digitally, and hence the data is actually discrete, i.e. $D(s_n, t_k)$ exists for specific $n, k \in \mathbb{N} \cup \{0\}$. From the discrete data, the imaging surface will be recovered.

Since the antenna emits long signals, linear chirps are the most commonly used signals in SAR, it is impossible to read travel times from the data and hence the data is pulse compressed by *match-filtering* it with conjugated and time-reversed signal transmitted by the antenna which then allows for travel-time estimation. Appendix A presents linear chirps formally and shows the effect of match-filtering on them.

Additionally, the data is range compressed by centering the pulse compression around the round-trip travel time from the antenna to any fixed point in the imaging scene. This is computationally advantageous since it removes large phases from the data and allows for more stable computations [3]. The data compressions are performed simultaneously

$$D_r(s, t) = \int \overline{f(t' - t - \tau(s, \vec{\rho}_o))} D(s, t') dt' \text{ and}$$

where $\tau(s, \vec{\rho}_o) = 2|\vec{\mathbf{r}}_p(s) - \vec{\rho}_o|/c_o$ is the round-trip travel time from the antenna at position $\vec{\mathbf{r}}_p(s)$ at time s to point $\vec{\rho}_o$,

After this processing, the compressed data is used to render an image of the scene of which the waves scattered. This process is addressed in the following section.

1.2 Image Formation

The imaging scene now has to be reconstructed from the data. The imaging process can be summarized as follows: Because the data consists approximately of time-delayed copies of the transmitted signal, an image is obtained by synchronizing them with travel-times and adding them over the aperture.

An image at point $\vec{\rho}^{\mathcal{I}}$ can be calculated in the following way [3],

$$\mathcal{I}(\vec{\rho}^{\mathcal{I}}) = \int_{-S(a)}^{S(a)} D_r\left(s, \tau\left(s, \vec{\rho}^{\mathcal{I}}\right) - \tau\left(s, \vec{\rho}_o\right)\right) ds \quad (1.1)$$

where $S(a)$ is the slow time range over the aperture of length a .

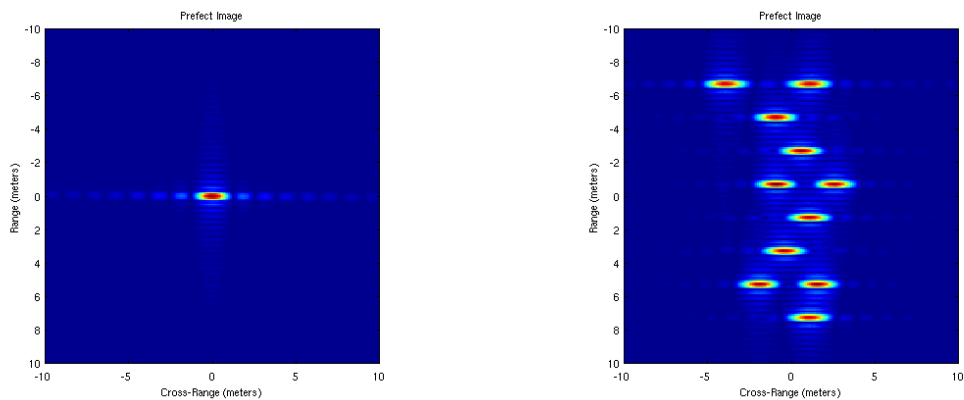
Since in a single pass of a standard SAR system there is not enough information for a three dimensional reconstruction of the imaging scene, then the standard practice in SAR is to assume that the imaging scene is flat, [8], and then to generate a grid of points in the region of interest and calculate the image on that grid. Without loss of generality, the imaging plane can be assumed to be at a height equal to 0, hence

$$\vec{\rho}^{\mathcal{I}} = (\rho_{X-R}^{\mathcal{I}}, \rho_R^{\mathcal{I}}, 0) \quad (1.2)$$

where $\rho_{X-R}^{\mathcal{I}}, \rho_R^{\mathcal{I}}$ are the cross-range and range components of $\vec{\rho}^{\mathcal{I}}$ respectively.

Figure (1.2(a)) shows an image of a stationary point-like target. Figure (1.2(b)) shows an image of multiple targets. The images were generated with simulated data using the same setup as in [3] for a particular SAR system known as Gotcha, see Appendix C for more the specific properties of this system. The specific parameters of this system are presented in appendix C. Both images corresponds to a single aperture of length $a = 124\text{m}$.

If the exact flightpath is known and all the targets within the imaging scene are stationary, the images produced will be focused. If, however, there is unaccounted motion, be it in the flightpath or on the ground, the images will not be focused. The scope of this thesis is to study the different algorithmic solutions given to the problem of having unaccounted motion in the flightpath. In the next section, a couple of examples of the image degradation that happens when the flightpath is not known completely are provided.



(a) Perfectly focused image of
a single point-like target

(b) Perfectly focused image of
multiple point-like target

Figure 1.2 : Perfectly focused images using one small aperture

1.3 Difficulties

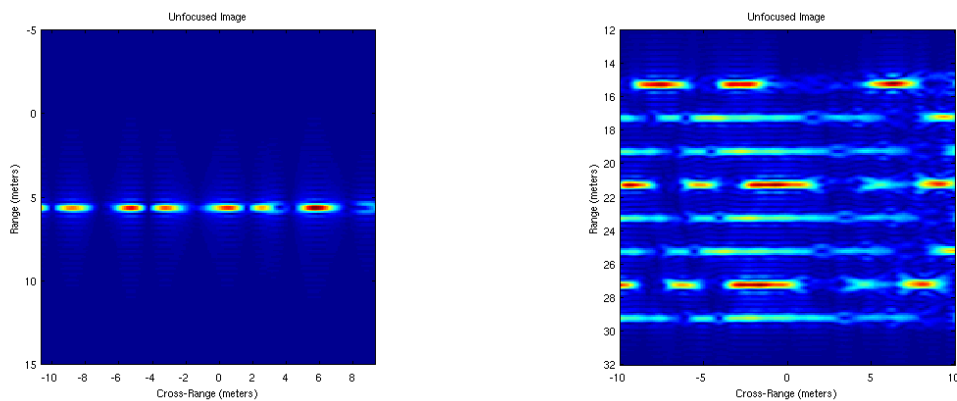
To render images, Equation (1.1) has to be synchronized within a wavelength otherwise, the images will be out of focus. Inexact knowledge of antenna position leads to imprecision in travel-times that could potentially be larger than a wavelength. For high resolution systems, such as Gotcha, the typical wavelength (λ_o) is in the order of centimeters ($\lambda_o \sim 3\text{cm}$ for the system in appendix C). The flightpath can be estimated by using GPS technology up to certain degree of accuracy which is often insufficient for proper synchronization.

The perturbations are of the form

$$\vec{\mathbf{r}}_p(s_i) + \vec{\boldsymbol{\mu}}(s_i) \quad (1.3)$$

for every firing time s_i where $\vec{\mu}(s_i)$ could be large with respect to the typical wavelength of a SAR system. Whilst very small perturbations can be neglected as they will not affect the image significantly, if the perturbations are sufficiently large, the images could be completely out of focus.

The effects of perturbations can be seen in Figure (1.3). For these images, the perturbations are of the order of one wavelength λ_0 , i.e. $|\vec{\mu}(s)| = O(\lambda_0)$. These two figures should be compared with Figures (1.2(a)) and (1.2(b)), which are images of the same scenes, respectively. As it can be observed the main loss of focus occurs in cross-range (along the x axis in this case).



(a) Unfocused image of a single point-like target (b) Unfocused image of multiple single point-like target

Figure 1.3 : Unfocused images using one small aperture.

It is evident that for there to be a successful rendition of the imaging scene, there has to be a sufficiently accurate knowledge of the travel times. If the perturbations

are estimated and compensated for, then, the images can be focused. This process is called *autofocus*. In the next section a brief history of SAR and some of the existing autofocus algorithms are presented.

1.4 Historical Developments

Synthetic Aperture Radar (SAR) was introduced to the scientific and engineering communities in 1960 as a collaboration between the University of Michigan and the U.S. Army [9]. This radar system was originally intended to improve the Azimuth resolution, the capability of distinguishing two targets close together in cross-range, of radar systems in existence at the time.

To attain higher resolution, the idea proposed was to synthesize a long antenna without actually building it. By mounting a smaller one on the side of a plane and having the plane follow a flightpath, an effective synthetic antenna could be created [9]. This synthesis allowed the new systems to create high-resolution images, using a simple flight path, which would have otherwise been impossible to obtain. Although the first successful image was generated in 1957, this new technology remained classified until 1960.

SAR, as any other radar system, relies on the reception and interpretation of waves scattered back from a target or multiple targets. Within the diverse Radar systems in existence, it is considered as an active system in that it provides its own illumination (generates its own signal) and consequently can operate at any time of day [8] which

makes it versatile for many applications of high-resolution daylight-independent imaging [25]. Additionally, as it records both the phase and the magnitude of the reflected signal, SAR is a coherent system [8].

Amongst the different SAR systems in existence, two main categories exist, Spotlight and Strip map SAR, [8]. In spotlight SAR, the antenna always illuminates the same location on the ground during the flight. In stripmat SAR, the antenna's illumination sweeps the ground following the flightpath, [7].

Since for ultra-high resolution images, short wavelength signals have to be used, small perturbations to the flightpath can cause severe problems in the image reconstruction. Hence it became paramount to the development of the technique that some way of focusing the images were devised.

The most celebrated method of automatically focusing the data is known as *phase gradient autofocus* (PGA) and it was introduced in [13]. Since then, many of the autofocus algorithms have been extensions of this method.

About a decade later, an optimization based method that uses entropy as a measurement of image contrast for autofocus was introduced in [24] and later in [21] the ideas were extended to more general image contrast metrics. The main limitations of these methods are those of non-convex optimization in high dimensions.

Recently a somewhat different approach using Wigner transforms and ambiguity functions is employed in [3]. The use of the Wigner transform had already been proposed for velocity estimates in [2] and also used in [11] and [10] but not for the

autofocus problem and with the analysis from first principles shown in [3].

In the following chapters, three different algorithms to solve the autofocus problem will be compared side by side on both simple and complex imaging scenes with increasing levels of perturbations in the flightpath.

Chapter 2

Autofocus

The purpose of autofocus techniques is to compensate for the imprecision of travel-times that do not take into account the flightpath perturbations. If an autofocus algorithm is successful, the SAR images produced will be focused. In this chapter, three different methods will be explained and compared. The first one is the most popular focusing techniques, the phase gradient autofocus algorithm, and it was introduced in [12] and it has proven to be quite robust for most spotlight SAR imaging. The second one, image entropy minimization, was introduced in [24] and it belongs to more general series of algorithms based on measurements of image contrast [21]. The third one, the phase-space method, was introduced in [3]. It uses both the Wigner transform and the ambiguity function of the data for autofocus. Additionally, it provides an algorithm for target tracking (velocity estimation of a moving target) that can be used when no autofocus is required.

Section 2.1 will describe PGA, section 2.2 is devoted to the entropy based autofocus and section 2.3 presents the phase-space method along with a filter designed to attenuate high frequency perturbations.

The comparison is done using the Gotcha system described in Appendix *C* for a single point-like target scene with induced perturbations and a more complex scene

with multiple targets. The first two methods, PGA and the image entropy minimization, provide point-wise estimations of the perturbations for each slow time s . The Phase-Space Method, on the other hand, provides a parametric estimation of the magnitude of the perturbation, its speed and its acceleration, via a second order polynomial. That is, it approximates locally the flightpath, over a slow time interval by a polynomial of degree 2.

2.1 Phase Gradient Autofocus

In 1988 an automated algorithm, know as phase gradient autofocus (PGA), was proposed to focus data [12] by estimating and correcting phase errors for spotlight SAR [13]. The original algorithm used adjacent range-compressed image data to estimate the phase differences iteratively. More recently, the original PGA algorithm was shown to be particular case of a maximum-likelihood estimation of the phase errors, [5]. This maximum-likelihood estimation is now the most widely used version of PGA.

A schematic representation of the algorithm is shown in Figure 2.1, [5], [14]. An explanation of the steps will be presented after a brief discussion of the algorithmic assumptions.

Starting with the definition of two concepts: range and cross-range line. A range-line consists of all the data points that fall into the same fast-time bin over all the slow times. A cross-range line corresponds to the data acquired for a fixed slow-

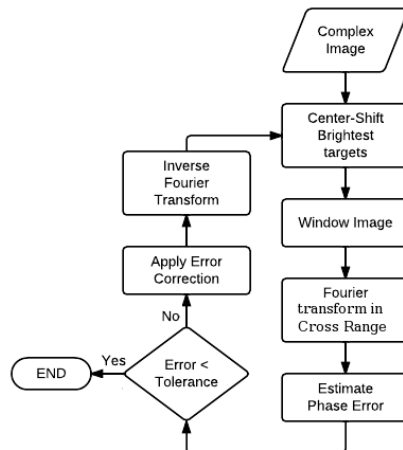


Figure 2.1 : Phase Gradient Autofocus Algorithm.

time. It is assumed that there exist only one main scatterer (target) per range-line and they are mutually independent across cross-range lines, i.e. the position of each scatterer in cross-range does not affect the position of any other target in cross-range. Figure 2.2 shows that situation where sufficiently separated point-like targets uniformly distributed in range produce data that can easily be binned together for each fast-time provided a sufficiently short aperture.

If the aperture is sufficiently small, an approximate image can be formed by Fourier transforming the data in both dimensions [15], [19]. For given data $\widehat{D}_r(s_k, \omega_m)$, where $k \in \{1, \dots, K\}$ refers to the cross-range index and $m \in \{1, \dots, M\}$, to the range index, the image is formed by, [4],

$$\mathcal{I}^F = \mathcal{FFT}_2 \left(\widehat{D}_r \right), \quad (2.1)$$

where \mathcal{FFT}_2 is the two-dimensional Fourier transform, resulting in an image \mathcal{I}_{km}^F ,

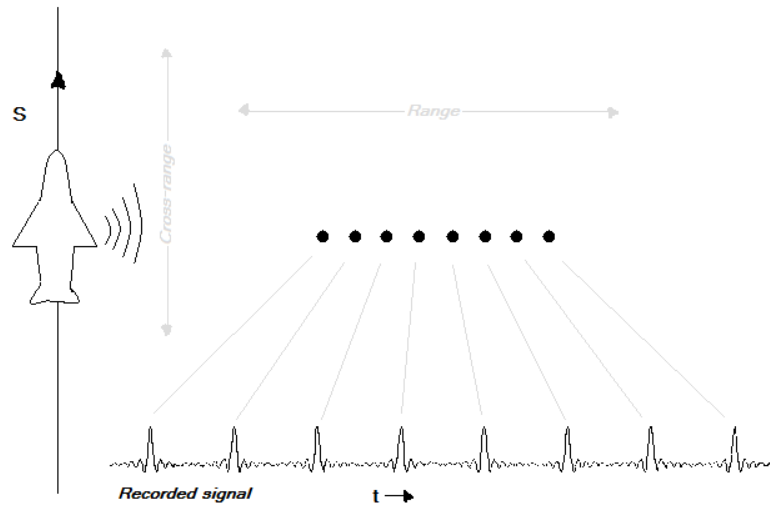


Figure 2.2 : Slow time / Fast time separation

for convenience of notation we shall omit the F superscript in the remainder of the section. As it should be expected, a Fourier transform based image is typically faster to compute via FFT's compared to Equation (1.1), [1] but an error is induced due to the lack of a uniform grid.

Algorithmic steps

The algorithm starts with an image that has already been formed which is a matrix denoted by \mathcal{I}_{km} where $k = 1, \dots, K$ corresponds to cross-range and $m = 1, \dots, M$ to range. The first step of the algorithm is to circular shift the main (brightest) scatterers to the center of the image along range-lines. Each range line is shifted independently and the number of bins it was shifted is recorded.

The second step is to then window in cross-range the shifted image around the

aligned targets to maximize the average target-to-clutter ratio to avoid the possible existence of other targets in the same range-line to affect the estimation of the phase error. This is done simply by zeroing out what is outside the central window. The window has to be chosen correctly to both avoid either discarding relevant phase information or adding too much noise to the phase estimation. It is standard practice for SAR imagery to use a $16dB$ threshold from the brightest point of the image in the azimuth direction, [17]. The windowed image shall be denoted by \mathcal{I}_{km}^w .

The third step is to Fourier transform \mathcal{I}_{km}^w along the cross-range (along k) direction but leaving the range one unaltered. The image after such a transformation is referred to as the *range-compressed phase-history domain*, [5] and it shall be denoted by $\tilde{\mathcal{I}}_{km}^w$. The range compressed domain can be seen as a rank one matrix (made of rows that are scaled version of each other) plus some complex noise i.e.

$$\left[\tilde{\mathcal{I}}^w\right] = [\vec{\mathbf{p}}\vec{\mathbf{a}}^T] + [\eta] \quad (2.2)$$

where $\vec{\mathbf{p}} = [1, e^{i\Psi_2}, \dots, e^{i\Psi_K}]^T$. Alternatively this relationship can be written as

$$\tilde{\mathcal{I}}_{km}^w = a_m e^{i\Psi_k} + \eta_{km}$$

where Ψ_k is the common phase of the data across cross-range lines that is at slow time k due to track perturbations, a_m is a scattering amplitude due to the target at range bin m and $[\eta]$ is complex with uncorrelated real and imaginary parts modeled as white noise, i.e.

$$[\eta] = [\eta_R] + i[\eta_I] \quad (2.3)$$

where

$$[\eta_R]_{km}, [\eta_I]_{km} \sim \mathcal{N}(\mu, \sigma). \quad (2.4)$$

Here the notation \sim means it is distributed according to a Gaussian distribution with some mean μ and some standard deviation σ , and each entry is independent of the others. Since now there is a distribution associated to the error, a statistical approach can be taken.

The fourth step is to estimate the phases of $\vec{\mathbf{p}}$. Let $\Psi = [\Psi_1, \Psi_2, \dots, \Psi_K]^T$ denote such phases. The estimation of the phases is done as to maximize the log-likelihood of range-compressed data $\tilde{\mathcal{I}}$ over the phases. If p denotes the density of the data, then, the density and the log-likelihood of the data given the phases can be written as

$$\begin{aligned} p(\tilde{\mathcal{I}}|\Psi) &= \frac{1}{((2\pi)^K |\mathbf{C}|)^M} e^{-\frac{1}{2} \sum_{m=1}^M \tilde{\mathbf{I}}_m^T \mathbf{C}^{-1} \tilde{\mathbf{I}}_m} \\ \ln p(\tilde{\mathcal{I}}|\Psi) &= -M \ln [(2\pi)^K |\mathbf{C}|] - \frac{1}{2} \sum_{m=1}^M \tilde{\mathbf{I}}_m^T \mathbf{C}^{-1} \tilde{\mathbf{I}}_m \end{aligned} \quad (2.5)$$

with \mathbf{C} being the covariance matrix of the range lines $\tilde{\mathbf{I}}_m = a_m e^{i\Psi}$ and $|\mathbf{C}|$ denoting its determinant. The idea is to find the phases Ψ that maximize the log likelihood of the current data. If these are estimated, they can be removed and the resulting image will be better focused. Hence the maximization can be formulated as

$$\Psi^* = \operatorname{argmax}_{\Psi} \ln p(\tilde{\mathcal{I}}|\Psi) \quad (2.6)$$

Since $|\mathbf{C}|$ is independent of Ψ , then relation (2.6) is equivalent to the following maximization problem which can be relaxed to a eigenvector calculation,

$$\Psi^* = \operatorname{argmax}_{\Psi} (e^{-i\Psi})^\top \mathbf{C} e^{i\Psi},$$

with the observation that now \mathbf{C} , and not \mathbf{C}^{-1} , appears.

Since \mathbf{C} is unknown, the empirical correlation matrix is used

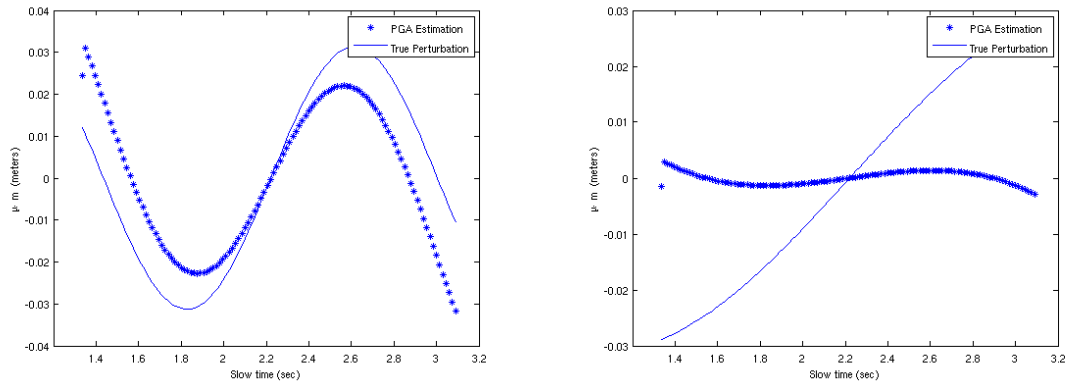
$$\hat{\mathbf{C}} = \frac{1}{M} \sum_{m=1}^M \tilde{\mathbf{I}}_m \tilde{\mathbf{I}}_m^\top.$$

This estimation has been shown to attain the Cramer-Rao lower bound on variance on real SAR data, [5].

The last step is to focus the data updating $\tilde{\mathcal{I}}_{km} \leftarrow \tilde{\mathcal{I}}_{km} \times e^{-i\hat{\Psi}_k^*}$ and inverse Fourier transforming the range-compressed phase-history domain back to an image. It should be noted that the correction is applied to the data without windowing, otherwise, information would be lost. Hence only phase information is updated. The process can be iterated until $e^{i\Psi_k} \approx 1, k = 1, \dots, K$, i.e. $\operatorname{mod}(\Psi_k, 2\pi) \approx 0$ for every k , where $\operatorname{mod}(\cdot, \cdot)$ is the modulus of the number, to some predetermined tolerance.

For a single scatter scene with a known platform perturbation of the form $\lambda_0 \sin(\gamma(s - s_o))$, the estimates rendered by PGA can be seen in Figure (2.3). In figure (2.3(a)), $\gamma = 4$, PGA produces a good estimate of the phase error and is hence able to focus the image. However, in figure (2.3(b)), where $\gamma = 4/3$, it seems at first sight that PGA does not capture the phase error correctly. This is actually not the case since the estimate produced by PGA captures most of the non-linear tendencies

in the error. Since the images are obtained by Fourier transforming the corrected data to an image, linear tendencies in the phase error only produce shifting in the position of targets in the image. They do not affect the focus.



(a) Recovered perturbation using PGA, $\gamma = 4$ (b) Recovered perturbation using PGA, $\gamma = 4/3$

Figure 2.3 : Phase error estimation using PGA

PGA is usually implemented to remove such linear tendencies from the phase estimation at every iteration [5]. This is done by fitting a line, in the least squares sense, to the pairs $(s_k, \hat{\Psi}_k)$ and subtracting it from $\hat{\Psi}$. Hence the phases recovered by PGA will only contain the non-linear parts of the estimates. Removing the linear tendencies in the phases also tries to minimize possible artificial shifting that the method could induce. PGA, then, needs additional information about the true location of at least one of the targets to correctly center the image, but the sharpness of the image is not affected by this.

2.1.1 Original algorithm

PGA can also be implemented by taking a partition of the slow-times and performing the estimate over each subset of slow times. Then, the estimates can be combined by adding them over each subset of slow-times. When only 2 contiguous slow-times are used for the estimation, the result of the eigenvalue problem is comparable to that of the first PGA algorithm proposed, [12]. In this setting, only two adjacent cross-range lines are considered, hence what is obtained is the phase difference between them, i.e. for cross-range lines ℓ and $\ell + 1$, $\Delta\Psi_\ell = \Psi_{\ell+1} - \Psi_\ell$

$$\widehat{\Delta\Psi}_\ell = \angle \left(\sum_{m=1}^M \tilde{\mathcal{I}}_{\ell,m} \tilde{\mathcal{I}}_{\ell+1,m} \right).$$

Where \angle denotes the principal value of the argument of the complex number. This is done for each pair over the entire cross-range. Since the algorithm relies only on phase differences, the first azimuth line can assigned a phase value of zero. The estimated phase correction can be recovered by simple addition

$$\widehat{\Psi}_l = \sum_{\ell=1}^{l-1} \widehat{\Delta\Psi}_{\ell+1}$$

The phase update is the same as above. While this case is less computationally demanding per iteration, it requires more iterations to reduce the phases sufficiently, [5]. By defining

$$\hat{\epsilon}_l = (\Psi_{l+1} - \Psi_l) - \widehat{\Delta\Psi}_l,$$

the following error estimation can be made,

$$\Psi_l - \widehat{\Psi}_l = \sum_{\ell=1}^{l-1} (\Psi_{\ell+1} - \Psi_\ell) - \sum_{\ell=1}^{l-1} \Delta \widehat{\Psi}_\ell = \sum_{\ell=1}^{l-1} \widehat{\epsilon}_\ell. \quad (2.7)$$

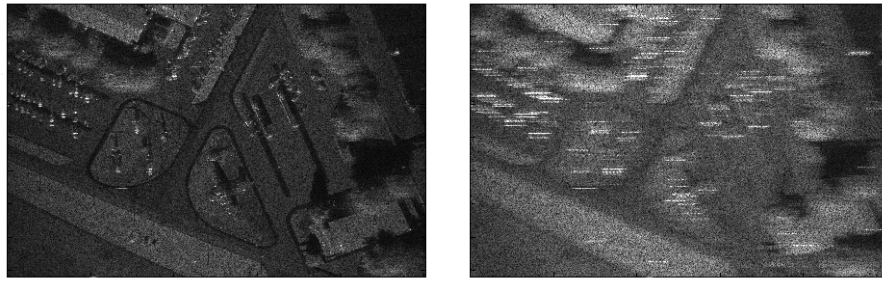
If the error is not zero mean, then there is a linear tendency introduced into the estimation which is addressed by removing all linear trends from the estimation.

2.1.2 Examples and difficulties

As an example of the performance of the PGA, Figure 2.4(a) shows a focused image of real SAR data, obtained from Sandia National Labs. Figure 2.4(b) shows a blurred image of the same scene. Figure 2.4(c) shows the result of applying PGA for the case $M = 2$ after 6 iterations.

After a series of numerical experiments, it was empirically observed that even if all the steps in the algorithm are performed properly, the method can still fail to focus the data. The reason behind the majority of the failures in the simulations was due to the presence two very similar targets aligned in cross-range within the window. That is, if two very similar (highly correlated) and aligned in range target patterns exist, the method will render an unfocused image. This suggests that the windowing should be made smaller at the risk of removing too much phase information of the image. Hence, this empirically suggests that applying the same windowing criterion to all images might lead to some images not to be focused.

In the next section, a different idea, a contrast-metric based optimization method will be presented.



(a) Original focused image

(b) Blurred image



(c) Image deblurred by PGA

Figure 2.4 : PGA example using Sandia National Laboratories SAR imagery

2.2 Contrast-metric method

Contrary to PGA that uses the redundancy of the phases in the range-compressed phase-history domain, contrast-metric based algorithms use a proxy for the focus of the image and then use optimization tools to focus the image via that proxy. In [24], an algorithm that minimizes the entropy of the image, in the sense of Shannon [22], was proposed to improve focus. This algorithm assumes, in the same fashion as PGA, that the focusing is done by correcting phases that are common for each cross-range line in the phase-history domain. It was later shown that this algorithm was a part of

a more general collection of algorithms that focus SAR images based on any metric of sharpness [21].

The basic assumptions are as follows. Once again, the flightpath $\vec{\mathbf{r}}_p(s)$ is assumed to be a straight path, if not, a change of variables is performed. An image is formed by Fourier transforming the data in both frequency and slow time as in Equation (2.1).

In this section, the notation for the data and the images will be different from the previous section, mainly due to the fact that there is no windowing or shifting performed. Let $\mathcal{Z}_{km} = \mathcal{Z}(\xi_k, t_m)$ be the (k, m) pixel of the unfocused complex image where k and m correspond to cross-range and range respectively. By taking a Fourier Transform in cross-range of the unfocused image (landing in the range-compressed phase history domain), denoted by $\tilde{\mathcal{Z}}_{km}$, then a relationship with the perfectly focused image can be established. Let \mathcal{I}_{km} be the focused complex image, ($\tilde{\mathcal{I}}_{km}$ after taking Fourier Transform in cross-range) then, following relationships is assumed hold

$$\tilde{\mathcal{Z}}_{km} = e^{i\phi_e^k} \tilde{\mathcal{I}}_{km}, \forall m = 1, \dots, M, \text{ and } k = 1, \dots, K$$

where ϕ_e^k is the unknown phase error that only depends on cross range because cross-range is affected by the precision of the knowledge of the track as seen in figures 1.3. The problem now becomes to find \mathcal{I}_{km} given only \mathcal{Z}_{km} . This estimate can be expressed in terms of matrices in the following way

$$\hat{\mathcal{I}}(\vec{\phi}) = \mathcal{F}\mathcal{F}\mathcal{T}_k \left(\text{diag} \left[e^{-i\vec{\phi}} \right] \tilde{\mathcal{Z}} \right),$$

where $\vec{\phi} = (\phi_1, \dots, \phi_N)$ is a phase correction, $diag [e^{-i\vec{\phi}}]$ is a diagonal matrix with $e^{-i\phi_k}$ as it's diagonal elements, $\widehat{\mathcal{I}}$ is the image as focused by the phase correction and after applying discrete Fourier Transform in cross-range (\mathcal{FFT}_k) of the unfocused image corrected by the phase.

It is clear that \mathcal{I} is not known and hence what is usually done is to find $\vec{\phi}^*$ such that

$$\vec{\phi}^* = \arg \min_{\vec{\phi} \in [0, 2\pi]^N} \Phi \left(\widehat{\mathcal{I}} \left(\vec{\phi} \right) \right) \quad (2.8)$$

for some function Φ that acts as a way of measuring the sharpness of the image. For simplicity, the explicit dependency on the image will be dropped, i.e.

$$\Phi \left(\vec{\phi} \right) = \Phi \left(\widehat{\mathcal{I}} \left(\vec{\phi} \right) \right). \quad (2.9)$$

As with any optimization problem when the objective function is not sufficiently well behaved, it is possible for any optimization algorithm to find a local minimum which will not necessarily render a focused image.

2.2.1 Entropy based autofocus

The entropy of an image is a measurement of the contrast there exist between the intensities of the pixels. Hence a focused image should have lower entropy than an unfocused one. The assumption is that the entropy of the image is the lowest when it is perfectly focused. With this idea, [24] proposes to find the phase vector that minimizes this measurement and thus focus the images.

For this case, the function $\Phi(\vec{\phi})$ will be the entropy of the focused image and it can be expressed in terms of the following quantities:

$$\begin{aligned}\mathcal{E}_{\hat{\mathcal{I}}} &= \|\hat{\mathcal{I}}\|_F^2 = \sum_{k,m} \hat{\mathcal{I}}_{km} \overline{\hat{\mathcal{I}}_{km}} \\ \Phi(\vec{\phi}) &= - \sum_{k,m} \frac{\hat{\mathcal{I}}_{km} \overline{\hat{\mathcal{I}}_{km}}}{\mathcal{E}_{\hat{\mathcal{I}}}} \log \left(\frac{\hat{\mathcal{I}}_{km} \overline{\hat{\mathcal{I}}_{km}}}{\mathcal{E}_{\hat{\mathcal{I}}}} \right)\end{aligned}$$

With this particular choice of metric, the optimization can be done directly and even first-order optimization methods can be readily used since $\Phi(\vec{\phi})$ is differentiable and the ℓ -th component of its gradient is given by

$$\begin{aligned}\frac{\partial \Phi}{\partial \phi_\ell}(\vec{\phi}) &= \frac{2}{N \mathcal{E}_{\hat{\mathcal{I}}}^2} \left\{ \sum_{a,b} \text{Im}(\eta_{abl}) \sum_{k,m} \hat{\mathcal{I}}_{km} \overline{\hat{\mathcal{I}}_{km}} \log(\hat{\mathcal{I}}_{km} \overline{\hat{\mathcal{I}}_{km}}) \right. \\ &\quad \left. - \mathcal{E}_{\hat{\mathcal{I}}} \sum_{k,m} \text{Im}(\eta_{km\ell}) \log(\hat{\mathcal{I}}_{km} \overline{\hat{\mathcal{I}}_{km}}) \right\}\end{aligned}\quad (2.10)$$

where $\eta_{abl} = \hat{\mathcal{I}}_{ab} e^{-i2\pi lb/K} e^{-i\phi_\ell} \overline{\hat{\mathcal{I}}_{la}}$. Even though this seems like a straight forward optimization problem, if the images are sufficiently large, this can become intractable for most computers. Since the optimization is performed over each cross-range line, there are as many variables in the search space as there are cross-range lines (slow-times). Hence even for relatively small pictures the optimization can be very time-consuming.

2.2.2 Implementation

To address the computational burden of high dimensional optimization, a simplified coordinate descent method was proposed in [16]. The idea behind this method is to

use a first degree Taylor approximation to the entropy function as a *surrogate* function that is easier to optimize and then to use a coordinate descent iterative method to find the optimum phase correction. In this case the function being optimized at the l -th iteration will be

$$\Theta(\vec{\phi}, \vec{\phi}^{(l)}) = -1/\mathcal{E}_{\hat{\mathcal{I}}} \sum_{n,m} \left| \hat{\mathcal{I}}_{km} \right|^2 \log \left| \hat{\mathcal{I}}_{km}^{(l)} \right|^2 + \log(\mathcal{E}_{\hat{\mathcal{I}}}). \quad (2.11)$$

where $\hat{\mathcal{I}}_{km} = \hat{\mathcal{I}}_{km}(\vec{\phi})$ and $\hat{\mathcal{I}}_{km}^{(l)} = \hat{\mathcal{I}}_{km}(\vec{\phi}^{(l)})$.

This optimization is done sequentially for each ϕ_ℓ in the usual coordinate-descent fashion. Let $\psi(\phi_\ell) = \Theta(\vec{\phi}, \vec{\phi}^{(l,\ell)})$ where

$$\vec{\phi}^{(l,\ell)} = \left(\phi_1^{(l+1)}, \dots, \phi_{\ell-1}^{(l+1)}, \phi_\ell, \phi_{\ell+1}^{(l)}, \dots, \phi_K^{(l)} \right).$$

So the interest is to calculate

$$\phi_\ell^{(l+1)*} = \arg \min_{\phi_\ell} \psi(\phi_\ell) \quad (2.12)$$

which has an exact solution. By writing

$$\psi(\phi_\ell) = A_\ell \cos(\phi_\ell - \phi_\ell^{(l)}) + B_\ell \sin(\phi_\ell - \phi_\ell^{(l)}) + C_\ell \quad (2.13)$$

where

$$A_\ell = -\psi''(\phi_\ell^{(l)})$$

$$B_\ell = \psi'(\phi_\ell^{(l)})$$

$$C_\ell = \psi(\phi_\ell^{(l)}) + \psi''(\phi_\ell^{(l)})$$

then the solution to equation (2.12) is given by

$$\phi_\ell^{(l+1)} = \phi_\ell^{(l)} + \tan^{-1}(B_\ell/A_\ell) \quad (2.14)$$

and the image can be sequentially focused by

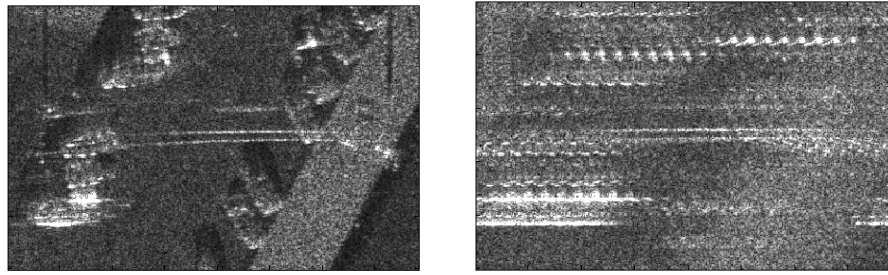
$$\widehat{\mathcal{I}}_{km}^{(l,\ell+1)} = \widehat{\mathcal{I}}_{km}^{(l,\ell)} + \frac{1}{N} e^{i2\pi\ell n/N} \left(e^{i\phi_\ell^{(l+1)}} - e^{i\phi_\ell^{(l)}} \right) \widehat{\mathcal{I}}_{km}^{(0,0)} \quad (2.15)$$

where $\widehat{\mathcal{I}}_{km}^{(0,0)} = \mathcal{Z}_{km}$. This entropy-based method can be viewed as a solution to a particular form of a multichannel problem [21]. Using these multichannel ideas, a slightly different algorithm using low rank approximations was proposed in [20]. However, the formulations lead to the same optimization problem and hence are no different than the one presented.

2.2.3 Examples and difficulties

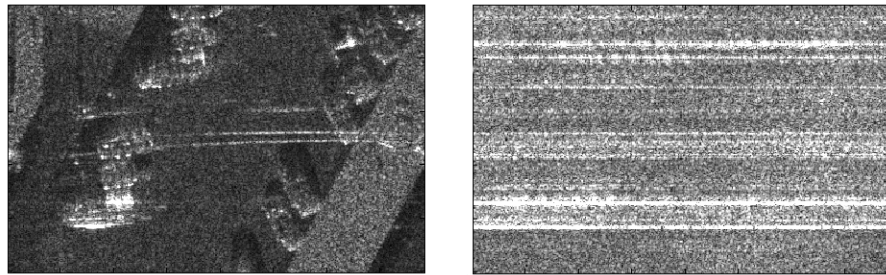
A small section of the image used for illustration of a complex scene for PGA is shown in figure (2.5). The reason to choose a smaller image is that the computational time is too long for such large apertures (2,500 slow-times). Figure (2.5(c)), the algorithm is able to focus an artificially blurred image. However, the algorithm depends on the starting point of the minimization since for (2.5(c)) the initial phases are all the same but for (2.5(d)), a random vector of phases was selected and there was no real improvement to the image.

Since the entropy of an image is invariant under circular shifts of the image, image-entropy minimization cannot hope to recover linear tendencies in the phase



(a) Original focused image

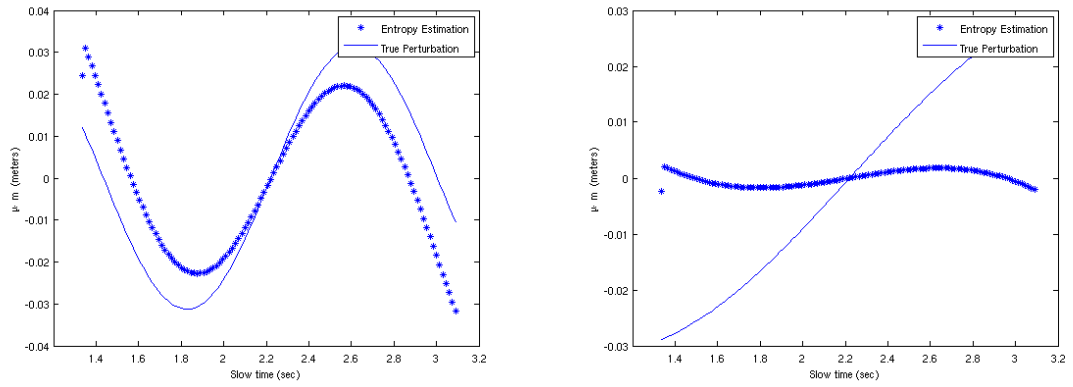
(b) Blurred image

(c) Image deblurred using $\phi_\ell = \pi$ as starting point

(d) Focus attempt using random starting point

Figure 2.5 : Entropy based autofocus example using Sandia National Laboratories SAR imagery

error. Hence this method will also need additional information on the position of at least one target in the scene to be able to center the image. Contrary to PGA, image-entropy minimization does not require the presence of only one dominant scatterer per range-line (fixed fast-time). Figure (2.6(a)) and (2.6(b)) show the phase recovered by image-entropy minimization method for perturbations of the form $\lambda_0 \sin(\gamma(s - s_o))$. For figure, (2.6(b)), it can be seen that the linear tendencies in the phase error are not quite captured by the method.



(a) Recovered perturbation minimizing entropy, (b) Recovered perturbation minimizing entropy,

$\gamma = 4$

$\gamma = 4/3$

Figure 2.6 : Phase error estimation Minimizing Entropy

In the next section, a non parametric approach to the phase error estimation, called the Phase-space method, is presented.

2.3 Phase-space based autofocus

The use of the Wigner transform for SAR estimations was introduced in [2] and it was originally used to detect and focus moving targets. This transform is also used in [11] and [10] for focusing moving targets. More recently, [3] studied in detail the use of both the Wigner transform and the ambiguity function of SAR data for autofocus and target tracking in SAR. The method in [3] allows for flightpath error compensation when the target is stationary. Conversely, if the flightpath is known, [3] presents an algorithm that allows for estimation of target velocity.

This thesis will only focus on the autofocus algorithm presented in [3] and it shall be referred to as the Phase space method.

The ambiguity function and the Wigner transform of the range-compressed data $\widehat{D}_r(s, \omega)$, as defined in [3], are, respectively,

$$\mathbb{A}(s, \Omega, \tilde{s}, T) = \int_{\omega_o - \pi B}^{\omega_o + \pi B} d\omega \int_{-\bar{S}}^{\bar{S}} d\tilde{s} \widehat{D}_r\left(s + \bar{s} + \frac{\tilde{s}}{2}, \omega\right) \overline{\widehat{D}_r\left(s + \bar{s} - \frac{\tilde{s}}{2}, \omega\right)} e^{i\bar{s}\Omega - i(\omega - \omega_o)T}, \quad (2.16)$$

$$\mathbb{W}(s, \Omega, \omega, T) = \int_{-\tilde{\Omega}}^{\tilde{\Omega}} d\tilde{\omega} \int_{-\bar{S}}^{\bar{S}} d\tilde{s} \widehat{D}_r\left(s + \frac{\tilde{s}}{2}, \omega + \frac{\tilde{\omega}}{2}\right) \overline{\widehat{D}_r\left(s - \frac{\tilde{s}}{2}, \omega - \frac{\tilde{\omega}}{2}\right)} e^{i\tilde{s}\Omega - i\tilde{\omega}T} \quad (2.17)$$

with Ω and T the dual variables to \bar{s} and $\omega - \omega_o$, respectively, in the ambiguity function and to \tilde{s} and $\tilde{\omega}$ in the Wigner transform. The limit of integration, in the Wigner transform, $\tilde{\Omega}$ is chosen so that $\omega \pm \tilde{\omega}/2$ remains in the support of \widehat{D}_r , i.e. $\tilde{\Omega} = 2\pi B - 2|\omega - \omega_o|$. By taking $\tilde{S} = a/(2V)$, the Wigner transform uses more than a single sub-aperture. This is also true for the ambiguity function if $\bar{S} = a/(2V)$.

Unlike the previously presented methods, the Phase space method provides a parametric estimation the actual perturbations to the flightpath over a small sub-aperture a . That is, it approximates locally the flightpath over slow time by a polynomial of degree 2. That is, the approximation is of the form

$$\vec{\mu}(s) \simeq \vec{c}_0 + \vec{c}_1 s + \vec{c}_2 s^2. \quad (2.18)$$

where \vec{c}_0 , \vec{c}_1 and \vec{c}_2 constant vector coefficients.

Additionally, even though the Wigner transform and the ambiguity functions are four-dimensional functions they have well defines peaks when the correct parameters are chosen, [3]. The location of these peaks can be used to obtain information about the trajectory of the antenna. The need for a quadratic approximation of the perturbation comes from the clear existence of the peaks in the transforms when this approximation is sufficiently good. However, there is not enough information in the data to be able to estimate all the entries of the vector coefficients in Equation 2.18, but as it is shown in [3], this is not necessary.

The peaks of the transforms can be used to estimate

- $\vec{\mu}(s_c) \cdot \vec{m}_o(s_c)$,
- $\vec{\mu}'(s_c) \cdot \vec{m}_o(s_c)$, and
- $\vec{\mu}''(s_c) \cdot \vec{m}_o(s_c)$

where s_c refers to center of the sub-aperture and

$$\vec{m}_o(s) = (\vec{r}_p(s) - \vec{\rho}_o) / |\vec{r}_p(s) - \vec{\rho}_o|. \quad (2.19)$$

The perturbations affect the image as explained in Appendix D. Under certain conditions, these projections are sufficient to recover the main contributions of the perturbation to the focus of the images.

For a scene where there is only a single point-like target and if the perturbations to the flightpath can be reasonably approximated by a second degree polynomial, where reasonable will be explained later, the Wigner transform and the ambiguity function of the data will each have one dominant peak that is used by the algorithm. However, if multiple targets exist, there will be multiple peaks to each of the functions [3]. To solve this issue, an average of the peak locations, known as a centroid, is used in [3] for the estimation. It should be noted that the centroid corresponds to the peak location should there only be one target in the scene. The centroid for the Wigner transform $(\overline{\Omega^W}(s), \overline{T^W}(s))$ is defined as follows

$$\overline{\Omega^W}(s) = \frac{\int_{-\infty}^{\infty} d\Omega \int_{-\infty}^{\infty} dT \Omega \mathbb{W}(s, \Omega, \omega_o, T)}{\int_{-\infty}^{\infty} d\Omega \int_{-\infty}^{\infty} dT \mathbb{W}(s, \Omega, \omega_o, T)}, \quad \overline{T^W}(s) = \frac{\int_{-\infty}^{\infty} d\Omega \int_{-\infty}^{\infty} dT T \mathbb{W}(s, \Omega, \omega_o, T)}{\int_{-\infty}^{\infty} d\Omega \int_{-\infty}^{\infty} dT \mathbb{W}(s, \Omega, \omega_o, T)},$$

and the centroid for the ambiguity function is similarly defined.

Recalling from Equation (1.3) that the perturbations to the flightpath are denoted by $\vec{\mu}(s)$, then, the method produces

$$\vec{\mu}^{PS}(s) = \left[\varphi_0 + sV\varphi_1 + \frac{(sV)^2}{2}\varphi_2 \right] \vec{\mathbf{m}}. \quad (2.20)$$

Formally, the algorithm is presented in Algorithm 1. The algorithm can be summarized as follows: Using the transformations of the data, the centroids are evaluated

Algorithm 1 Estimate $\vec{\mu}(s)$

DATA: Range-compressed data $\widehat{D}_r(s, \omega)$

OUTPUT: Approximation of $\vec{\mu}(s)$

1. Calculate the centroids of the Wigner Transform and the Ambiguity functions

$$\overline{\Omega^W} = \frac{\int_{-\infty}^{\infty} d\Omega \int_{-\infty}^{\infty} dT \Omega \mathbb{W}(0, \Omega, \omega_o, T)}{\int_{-\infty}^{\infty} d\Omega \int_{-\infty}^{\infty} dT \mathbb{W}(0, \Omega, \omega_o, T)}, \quad \overline{T^W} = \frac{\int_{-\infty}^{\infty} d\Omega \int_{-\infty}^{\infty} dT T \mathbb{W}(0, \Omega, \omega_o, T)}{\int_{-\infty}^{\infty} d\Omega \int_{-\infty}^{\infty} dT \mathbb{W}(0, \Omega, \omega_o, T)},$$

$$\overline{\Omega^A} = \frac{\int_{-\infty}^{\infty} d\Omega \int_{-\infty}^{\infty} dT \Omega \mathbb{A}(0, \Omega, \frac{a}{2V}, T)}{\int_{-\infty}^{\infty} d\Omega \int_{-\infty}^{\infty} dT \mathbb{A}(0, \Omega, \frac{a}{2V}, T)}.$$

2. Estimate the coefficients - V denotes platform speed

$$\varphi_0 = -\frac{c_o \overline{T^W}}{2}$$

$$\varphi_1 = -\frac{\lambda_o}{4\pi V} \overline{\Omega^W}$$

$$\varphi_2 = -\frac{\lambda_o}{2\pi a V} \overline{\Omega^A}.$$

3. Estimate the perturbation

$$\vec{\mu}^{PS}(s) = \left[\varphi_0 + sV\varphi_1 + \frac{(sV)^2}{2}\varphi_2 \right] \vec{\mathbf{m}} \quad (2.21)$$

RETURN $\vec{\mu}^{PS}(s)$

for both the ambiguity function and the Wigner transform, with these centroids, the coefficients in Equation 2.20 are calculated by the following relationships

$$\begin{aligned}\varphi_0 &= -\frac{c_o}{2}\overline{TW} \\ \varphi_1 &= -\frac{\lambda_o}{4\pi V}\overline{\Omega^W} \\ \varphi_2 &= -\frac{\lambda_o}{2\pi aV}\overline{\Omega^A},\end{aligned}$$

where V is the platform speed.

With the estimate produced by the algorithm, $\vec{\mu}^{PS}(s)$, the travel times can be updated, that is,

$$\tau^{PS}(s, \vec{\rho}_o) = \frac{2}{c_o} \left| \vec{r}_p(s) + \vec{\mu}^{PS}(s) - \vec{\rho}_o \right|. \quad (2.22)$$

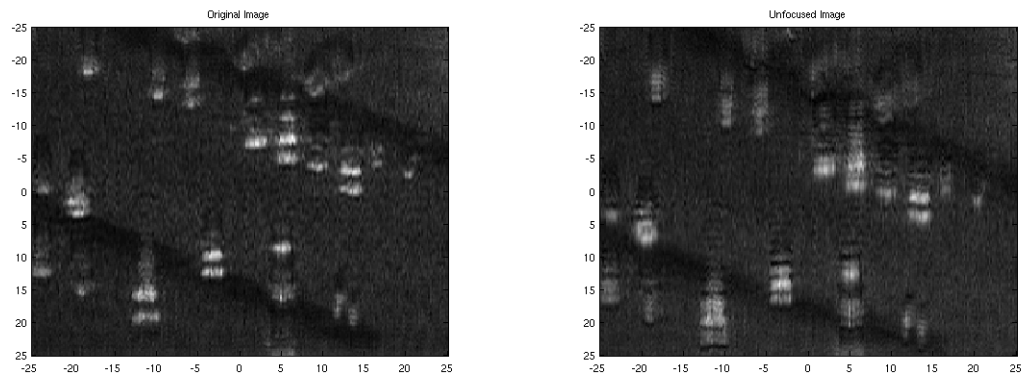
These updated travel times can then be used in the formation of images via Equation (1.1).

In the following section, a few examples of the performance of this method are presented.

2.3.1 Examples and difficulties

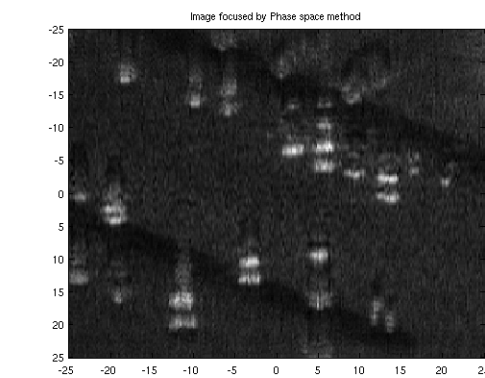
As an example of the performance of the phase-space method for a complex scene is shown in Figure (2.7). This is a sub-scene from the one used for PGA tuned for the size used with Gotcha parameters. Figure (2.7(b)) shows a blurred image of the same scene. Figure (2.7(c)) shows the result of applying the Phase-space method with induced perturbations. Since no flightpath information was available, an artificial

one was created with induced perturbations taking the information used for (2.8) for $\gamma = 2$



(a) Original focused image

(b) Blurred image



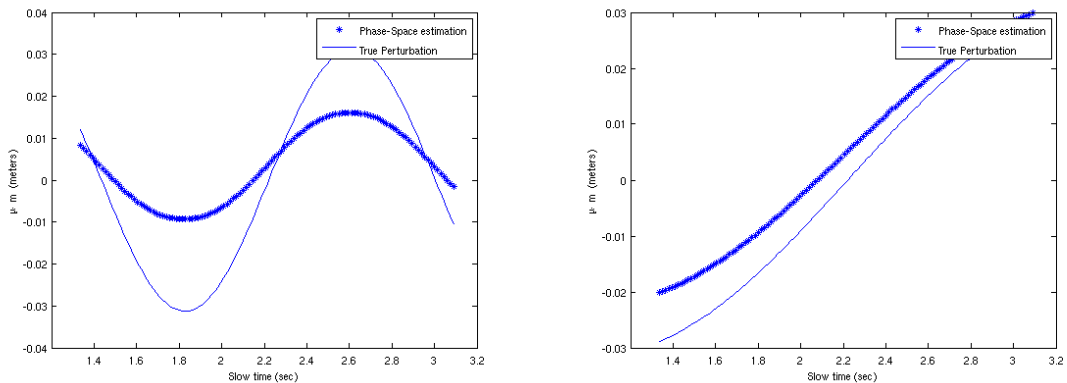
(c) Image deblurred by Phase-space method

Figure 2.7 : Phase-space method example using Sandia National Laboratories SAR imagery

If the perturbations are small enough, $|\vec{\mu}(s)| \ll \lambda_o$ then the effects on the images are negligible. However, when the magnitude of the perturbations becomes larger, i.e. $|\vec{\mu}(s)| \approx \lambda_o$ and the speed and acceleration bounds are violated (this happen when the

perturbations become rougher), then the phase-space method will produce estimates that cannot hope to capture the behavior of the perturbations. Intuitively, this is easy to understand since the estimation of rougher or highly oscillatory functions by means of a quadratic approximation is not very good.

For a single scatterer scene with a known platform perturbation of the form $\vec{\mu}(s) \cdot \vec{m}(s) = \lambda_0 \sin(\gamma(s - s_o))$, the estimates rendered by the phase space method can be seen in Figure (2.8). In figure (2.8(a)), $\gamma = 4$, in this case, the phase-space method is not able to recover the phase error due to the fact that a second degree polynomial is not sufficient to capture such type of perturbations. However in figure (2.8(b)), $\gamma = 4/3$, the Phase space recover the form of the perturbation quite well. Whilst there is a shift in the phase, that is known to have a negligible effect on the focusing of the image.



(a) Recovered perturbation using Phase Space Method, $\gamma = 4$ (b) Recovered perturbation using Phase Space Method, $\gamma = 4/3$

Figure 2.8 : Phase error estimation using the phase space method

If $\vec{\mu}(s)$ is very rough, then it cannot be approximated by a polynomial over an aperture of reasonable aperture needed by the Wigner transform and the ambiguity function. That is, for the approximation to be better the apertures has to be reduced and reduced until not enough is left for a proper estimation. In Figure (2.9) the Fourier transform of the data in slow time is used to show the effects of a very rough perturbation versus a smoother one for the central frequency ω_o . In the next section

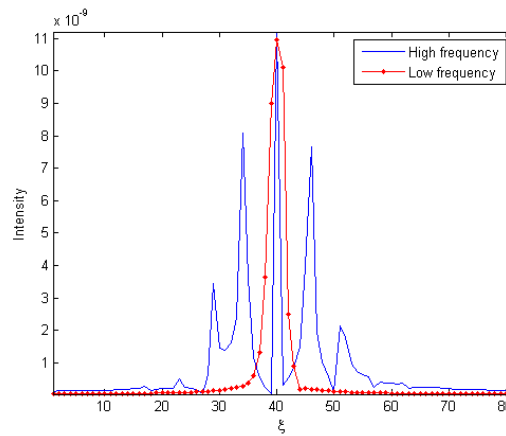


Figure 2.9 : Fourier transform in slow time of the data with different perturbations.

a filter will be proposed to smooth the track so that the phase space method can adequately capture the perturbation.

2.3.2 Bounds on approximation

The interest of this section is to devise a filtering criterion what will smoothen the track. The filtering is done by removing the high frequency components in the dual

variable to slow time so that the phase space method can capture the lower-frequency oscillations.

Recall from Algorithm 1 that the approximation is actually to $\vec{\boldsymbol{\mu}}(s) \cdot \vec{\boldsymbol{m}}(s)$ which comes out of the analysis in [3]. Since we can decompose $\vec{\boldsymbol{\mu}}(s) \cdot \vec{\boldsymbol{m}}(s)$ in its Fourier series, then, we look at platform perturbation of the form

$$\vec{\boldsymbol{\mu}}(s) \cdot \vec{\boldsymbol{m}}(s) = \alpha \lambda_0 \cos(\gamma(s + s_o)),$$

with $\alpha \in [0, 1]$ and γ the (angular) frequency of oscillation, which includes both sine and cosine cases.

Since the phase space method approximates the perturbations via a second degree polynomial, it is a relevant question what is the error that such an approximation produces in the presence of high frequency perturbations. To answer that question, first an ideal case should be considered, that is, what is the best approximating polynomial in an L^2 sense that can approximate the perturbations. The best approximations to $\vec{\boldsymbol{\mu}}(s) \cdot \vec{\boldsymbol{m}}(s)$ can be calculated by orthogonally projecting over that space of polynomial of degree up to 2. Given α , s_o and γ the best approximating quadratic function is then given by

$$\begin{aligned} \frac{1}{\alpha \lambda_o} \frac{2V}{a} p_2(s) &= s^2 \left(\frac{180V^3}{\gamma^2 a^3} \cos\left(\frac{a\gamma}{2V}\right) + \left(\frac{30V^2}{\gamma a^2} - \frac{360V^4}{\gamma^3 a^4} \right) \sin\left(\frac{a\gamma}{2V}\right) \right) \cos(\gamma s_o) \\ &+ s \left(\frac{6V}{\gamma a} \cos\left(\frac{a\gamma}{2V}\right) - \frac{12V^2}{\gamma^2 a^2} \sin\left(\frac{a\gamma}{2V}\right) \right) \sin(\gamma s_o) \\ &+ \left(\left(\frac{30V^2}{\gamma^3 a^2} - \frac{3}{2\gamma} \right) \sin\left(\frac{a\gamma}{2V}\right) - \frac{15V}{\gamma^2 a} \cos\left(\frac{a\gamma}{2V}\right) \right) \cos(\gamma s_o). \end{aligned} \quad (2.23)$$

It is important to notice that as $\gamma \rightarrow \infty$ then $p_2 \rightarrow 0$. Hence, for higher frequen-

cies, the residual $\epsilon_{\vec{\mu}} = \vec{\mu} \cdot \vec{\mathbf{m}} - p_2 \approx \vec{\mu} \cdot \vec{\mathbf{m}}$. We know that the Wigner transform will have a main peak for a single point-like target when the error is a quadratic function. However, when higher degrees appear, multiple peaks start appearing which makes the focusing fail. Hence, we should consider the cases when a single dominant peak appears in the Wigner transform. This can be done by studying the peaks of the Fourier transform of $e^{i\epsilon_{\vec{\mu}}/\lambda_o}$ in s . We consider first cubic polynomials for $\epsilon_{\vec{\mu}}$. From there we can *empirically observe* that the peak becomes non unique when $\|\epsilon_{\vec{\mu}}\| / \|p_2\| \gtrsim 1$. Figure (2.10) shows the magnitude of the Fourier transform of $e^{i\epsilon_{\vec{\mu}}}$ for 3 different settings

$$\|\epsilon_{\vec{\mu}}\| \approx 0.74 \|p_2\|$$

$$\|\epsilon_{\vec{\mu}}\| \approx 0.89 \|p_2\|$$

$$\|\epsilon_{\vec{\mu}}\| \approx 1.003 \|p_2\| .$$

As it can be readily observed, as $\|\epsilon_{\vec{\mu}}\|$ starts being large with respect to $\|p_2\|$, the magnitude of the Fourier transform of $e^{i\epsilon_{\vec{\mu}}}$ starts having multiple peaks of comparable height. This means that even for a single target, it could become impossible to correctly estimate the peak location that will effectively focus the image. Hence, the autofocus of the phase-space method will be better provided

$$\|\epsilon_{\vec{\mu}}\| / \|p_2\| \lesssim 1. \tag{2.24}$$

Consequently, the interest at hand is to find Γ such that

$$\frac{\|\epsilon_{\vec{\mu}}\|}{\|p_2\|} \lesssim 1$$

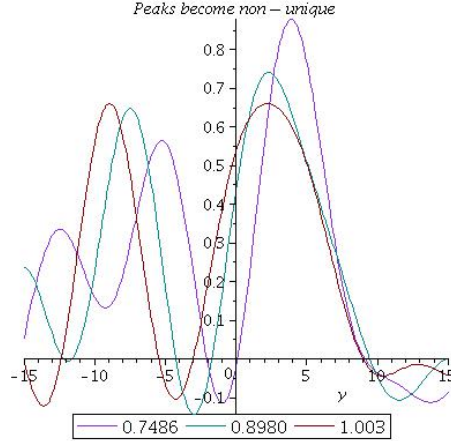


Figure 2.10 : No single peak appears when $\|\epsilon_{\vec{\mu}}\| / \|p_2\| \gtrsim 1$

for $\gamma \in [0, \Gamma]$. Since p_2 is an orthogonal projection over the space of polynomials of degree at most 2, then by orthogonality, $\|\epsilon_{\vec{\mu}}\|^2 = \|\vec{\mu} \cdot \vec{\mathbf{m}}\|^2 - \|p_2\|^2$, then this condition can also be formulated as $\|\vec{\mu} \cdot \vec{\mathbf{m}}\|^2 \lesssim 2 \|p_2\|^2$ for $\gamma \in [0, \Gamma]$. However,

$$-\frac{\alpha^2 \lambda_o^2}{2\gamma} \leq \|\vec{\mu} \cdot \vec{\mathbf{m}}\|^2 - \alpha^2 \lambda_o^2 \frac{2V}{a} \leq \frac{\alpha^2 \lambda_o^2}{2\gamma} \quad (2.25)$$

for $\gamma \geq 1$ and hence is bounded away from 0, a plot of this is shown in Figure (2.11(b)). Therefore the bound for the quotient will be violated when $2 \|p_2\|^2$ becomes smaller than the lower bound on $\|\vec{\mu} \cdot \vec{\mathbf{m}}\|^2$, i.e.

$$\|p_2\|^2 \leq \frac{\alpha^2 \lambda_o^2}{2} \left(\frac{2V}{a} - \frac{1}{2\gamma} \right). \quad (2.26)$$

In this case, finding Γ can be formulated as a root finding problem. Since $\|p_2\|^2 \rightarrow 0$ as $\gamma \rightarrow \infty$ and $0 \leq \frac{\alpha^2 \lambda_o^2}{2} \left(\frac{2V}{a} - \frac{1}{2\gamma} \right)$, then there exists one Γ such that

$$\|p_2\|^2 - \frac{\alpha^2 \lambda_o^2}{2} \left(\frac{2V}{a} - \frac{1}{2\gamma} \right) \leq 0 \quad (2.27)$$

for all $\gamma \geq \Gamma$. The numerical simulations performed empirically suggest to use the minimum γ where $\|p_2\|^2 = \frac{\alpha^2 \lambda_o^2}{2} \left(\frac{2V}{a} - \frac{1}{2\gamma} \right)$ which is again, a root finding problem.

2.3.3 Numerics for the filter

A few numerical experiments were done to find the cutoff of the frequencies that will allow for $\frac{\|\epsilon_{\vec{\mu}}\|}{\|p_2\|} 1$.

The plots are as follows, (2.11(a)) shows $\|\vec{\mu} \cdot \vec{\mathbf{m}} - p_2\|^2 / \|p_2\|^2$ as a function of γ for different shifts s_o . From it, it can be seen that for this particular setup of parameters, any $\gamma \geq 5.289$, violates the bound, shown by the dotted line and hence, the filter would have to at least remove all frequencies higher than that. Figure (2.11(b)) shows $\|\vec{\mu} \cdot \vec{\mathbf{m}}\|^2$ as a function of γ and the lower and upper bounds found in equation 2.25 for different values of s_o . As it can be seen, the norm always remains positive and bounded away from zero, which means that the polynomial has no hope of approximating it correctly. Lastly, Figure (2.11(c)) shows $\|p_2\|^2$ as a function of γ for different values of s_o along with the lower bound on the value of $\|\vec{\mu} \cdot \vec{\mathbf{m}}\|^2$. As it can be seen, for a sufficiently high value of γ , (2.11(c)) shows $\|p_2\|^2$ will be smaller than the lower bound and hence, the filter should any frequencies higher than that. It is immediate to see that the intersection of the different curves with the lower bound correspond to the point where the quotient condition is violated.

From these numerical results, we can design a filter that will zero out all data from frequencies higher than the bound. In this particular case, the filter should be

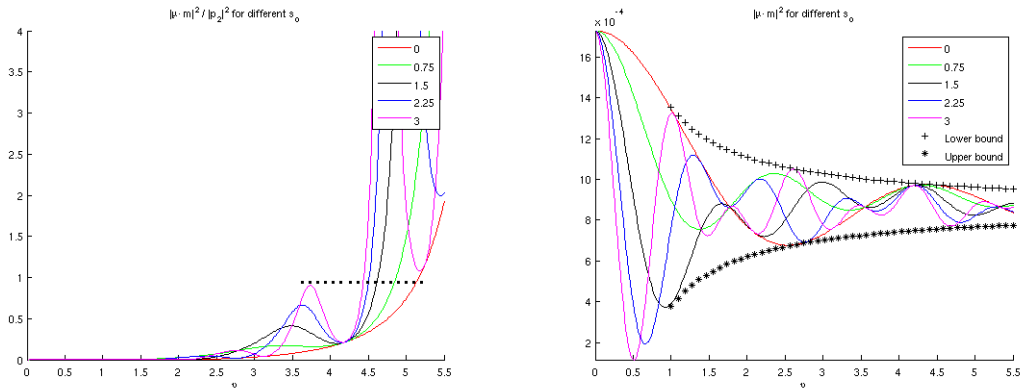
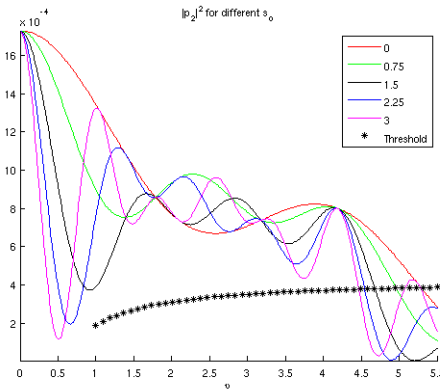
(a) $\|\vec{\mu} \cdot \vec{m} - p_2\|^2 / \|p_2\|^2$ as a function of γ (b) $\|\vec{\mu} \cdot \vec{m}\|^2$ as a function of γ (c) $\|p_2\|^2$ as a function of γ

Figure 2.11 : Phase error estimation using the phase space method

applied to $\gamma \geq 4.5$.

In the next section a few numerical comparisons are presented that test all the focusing methods for a single target scene with different perturbations.

Chapter 3

Numerical Comparison

In this chapter a series of different scenarios are presented with varying levels of noise both varying in amplitude and in frequency of their perturbations.

3.1 Direct comparison

The first series of plots correspond to the estimation done by the phase space method for single frequency perturbations, single-frequency noise, under three different amplitudes. The induced platform perturbations are of the form

$$\vec{\mu} \cdot \vec{\mathbf{m}}(s) = \alpha \lambda_0 \sin(\gamma s). \quad (3.1)$$

The comparison is as follows, the real perturbation is compared against the estimation provided by the Phase-space method, PGA for the full eigenvector problem, PGA for only contiguous slow-times (original version of PGA), and the Entropy-based minimization. The perturbation parameters are $\gamma = 1.33, 2, 4, 8$ and $\alpha = 1, 0.1, 0.01$. The implementation of PGA in its two modalities, and the Entropy-based minimization, were done by the author. As observed, the amplitude of the noise impacts significantly the quality of the image produced regardless of the autofocus technique used. The phase space method is initially applied without filtering to view the difficulties

it encounters, however, once the filtering takes place the images are focused.

In the case of low frequency, $\gamma = 1.33$, Figure (3.1), the initial images are quite good to begin with. All methods focus the image well. There are slight differences in the estimation of PGA and the Entropy-based minimization with respect to the real perturbation. The cause of this difference is that both PGA and the Entropy-based minimization do not have a way to account for the linear tendencies in the phase which just result in shifts in the image. However, as the frequency of the perturbations increases, the linear tendency of the perturbations converges to zero. The Phases-space method uses a good initial guess of the location of the target to recover the linear tendencies.

For $\gamma = 2$, Figure (3.1), the same behavior of the estimates is observed, however, the Entropy-based minimization reaches the maximum number of iterations allowed in the current implementation and so fails to recover the perturbation very well. Once again, the Phase-space method is the only one that recovers the linear tendencies of the perturbation. PGA is able to produce a good estimate only in its eigenvector formulation, while the contiguous version struggles to estimate the perturbations correctly when the amplitude is small. The Entropy-based minimization does remarkably well for small amplitudes.

For $\gamma = 4$, Figure (3.1), the Phase-space method already has reached its limit in terms of the frequencies it can estimate. The rest of the methods continue to perform similarly to the previous case. Once again, the Entropy-based minimization

does quite well for the smaller amplitudes.

For the last case, $\gamma = 8$, Figure (3.1), both the full eigenvector version of PGA and the Entropy-based minimization continue to render very precise estimates of the perturbation, specially for the smaller amplitudes. The Phase-space method is no longer working inside it's domain of estimation and the original PGA algorithm is also unable of correctly estimating the perturbations.

3.2 Effects of a adding the filter

The effect of filtering the data so that the Phase-space method can estimate the lower frequencies of the perturbations are shown in Figure (3.2). As it can be seen, the method can perform much better than before and now render focused images in the cases where it could not before.

3.3 Conclusions

As seen for SAR, as for any imaging method, focusing the images is crucial. The different focusing methods presented in this thesis had never been compared, side to side, before this work.

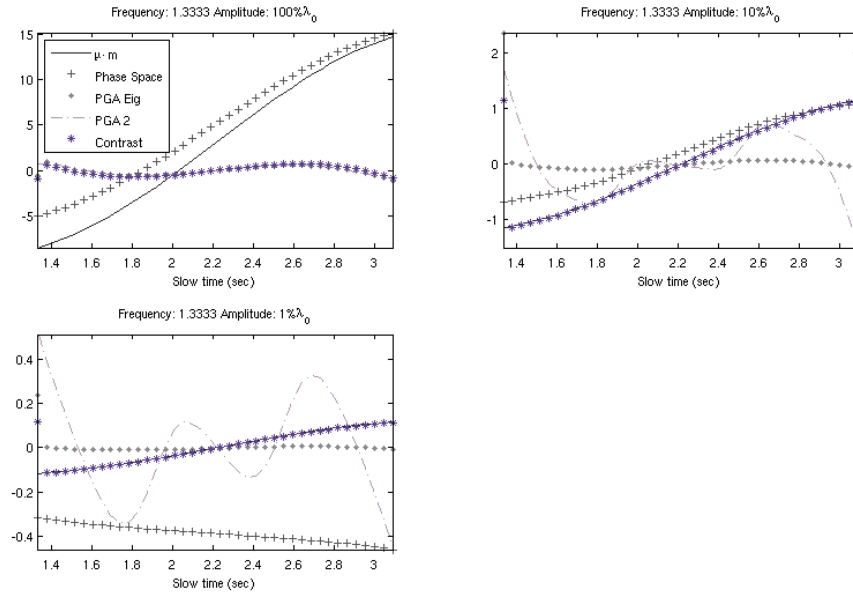
PGA is fast and effective but cannot focus images when there are scenes have strong targets at the same range (resolution size). The entropy-minimization algorithm is very good a capturing the perturbations but can be very slow for even not so large apertures. It is also heavily dependent on the starting point for the opti-

mization. Bad initial guesses lead to unfocused images. The phase-space method provides a parametric estimation of the platform perturbations that had not been done before and it is quite effective at estimating linear tendencies which none of the other methods can accomplish. It can focus multiple target images regardless of their position (within a certain imaging radius).

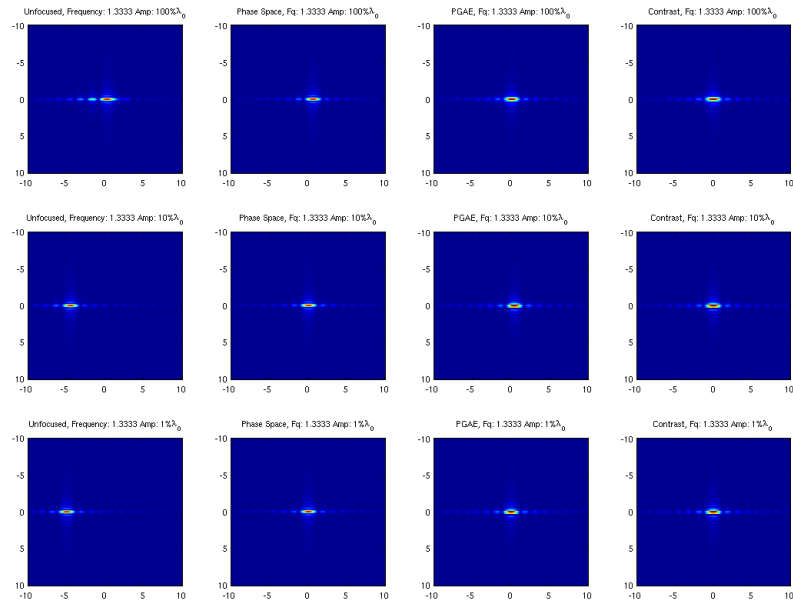
It should be noted that, unlike the other two methods, the phase-space method can alternatively be used to estimate the velocity of a target [3]. This makes this method more versatile for the usual SAR scenes that contain moving targets.

Additionally in this thesis we propose a filter to help the Phase-space method focus images when the perturbations are outside of the original scope of its intent for a fixed aperture.

This thesis also provides numerical examples for both simulated data and real SAR data to illustrate the different methods and compare their performance.

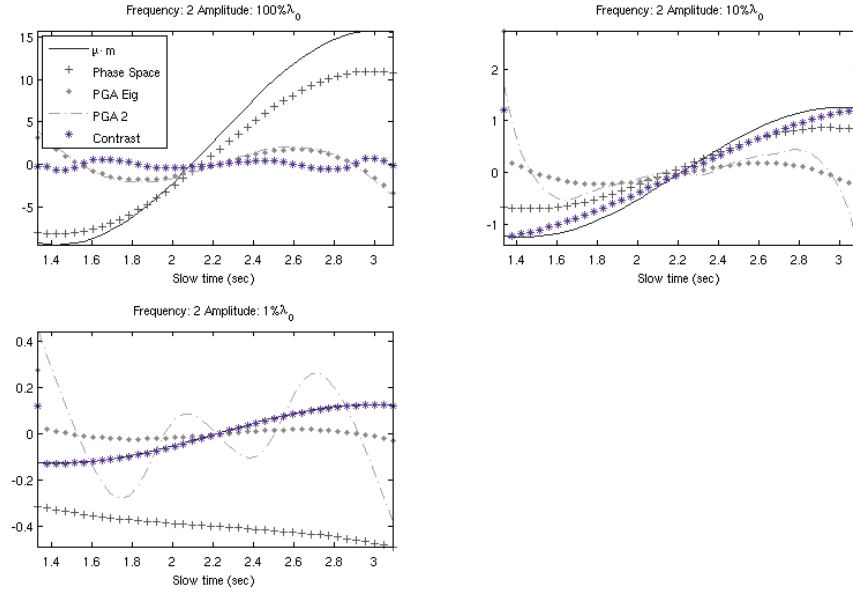


(a) Estimation for $\vec{\mu}(s) \cdot \vec{m}(s)$

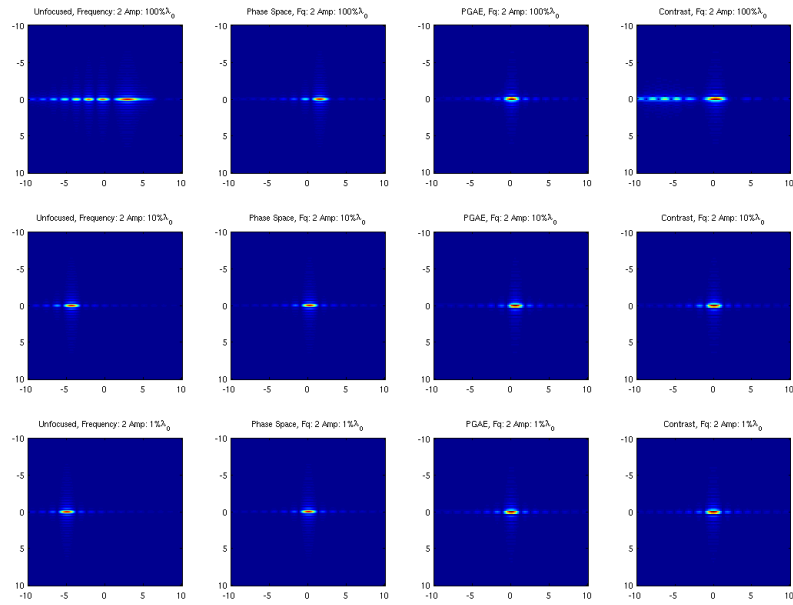


(b) Focused images

Figure 3.1 : Focusing by phase space method using sinusoidal noise, $\gamma = 1.33$

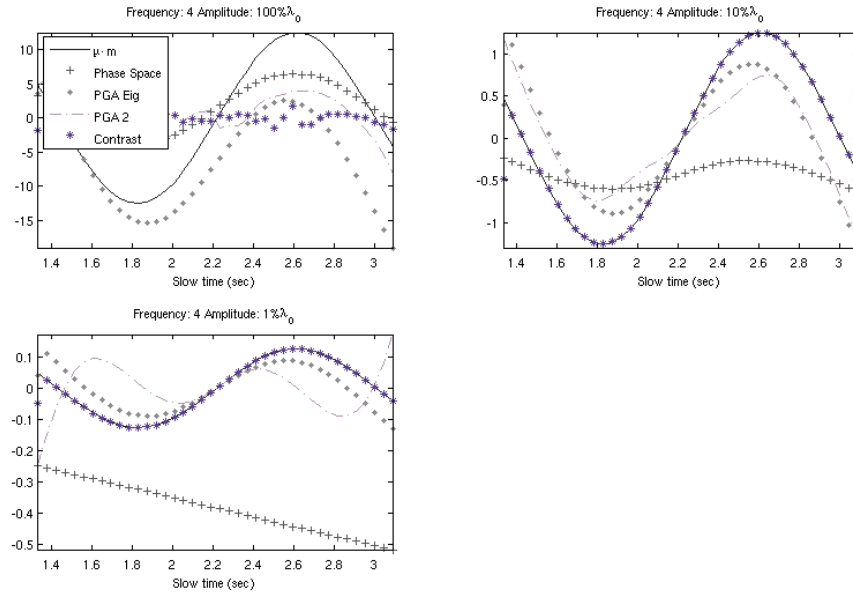


(a) Estimation for $\vec{\mu}(s) \cdot \vec{m}(s)$

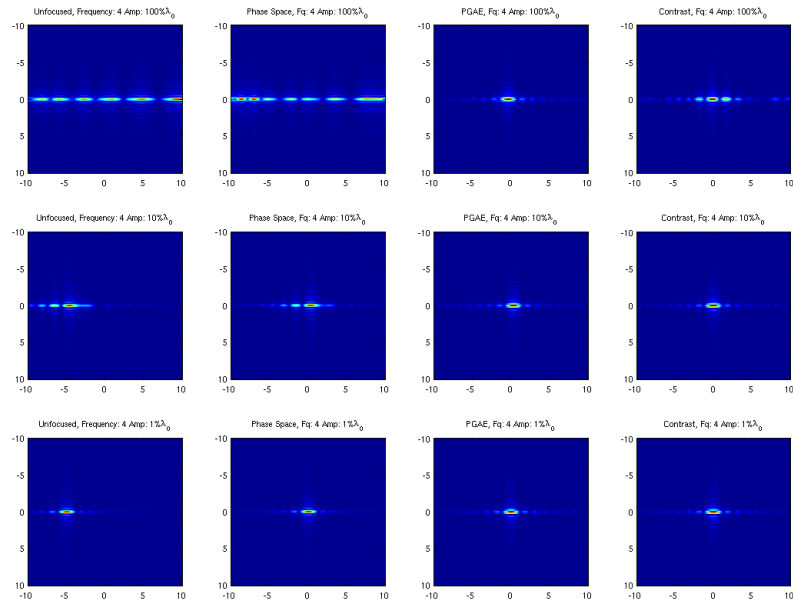


(b) Focused images

Figure 3.2 : Focusing by phase space method using sinusoidal noise, $\gamma = 2$

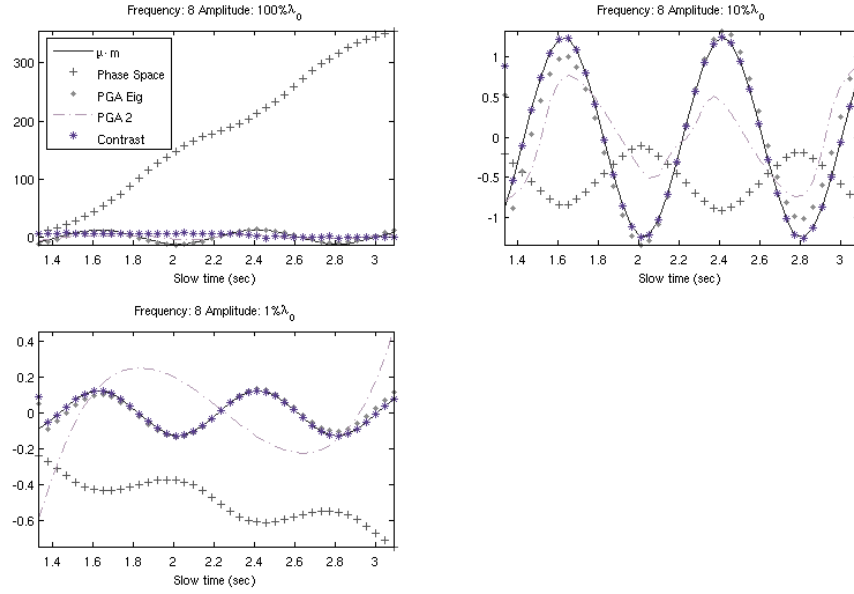


(a) Estimation for $\vec{\mu}(s) \cdot \vec{m}(s)$

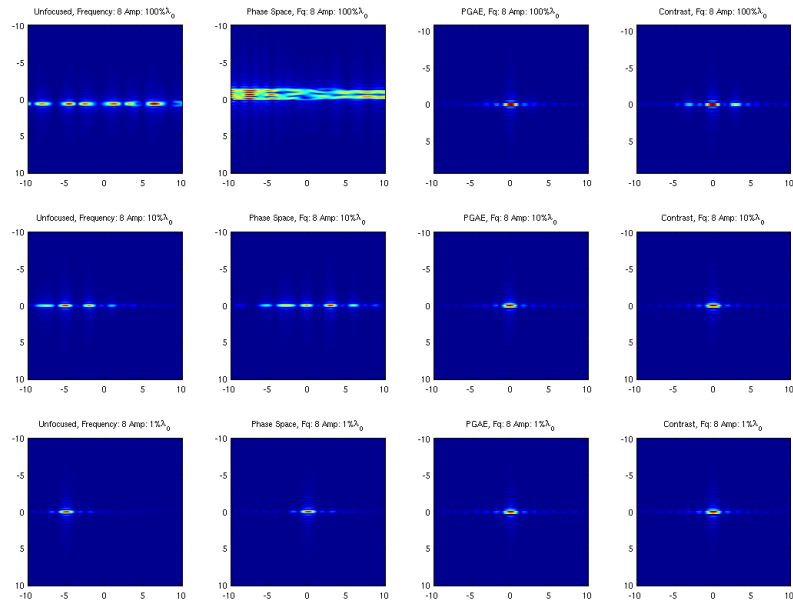


(b) Focused images

Figure 3.3 : Focusing by phase space method using sinusoidal noise, $\gamma = 4$



(a) Estimation for $\vec{\mu}(s) \cdot \vec{m}(s)$



(b) Focused images

Figure 3.4 : Focusing by phase space method using sinusoidal noise, $\gamma = 8$

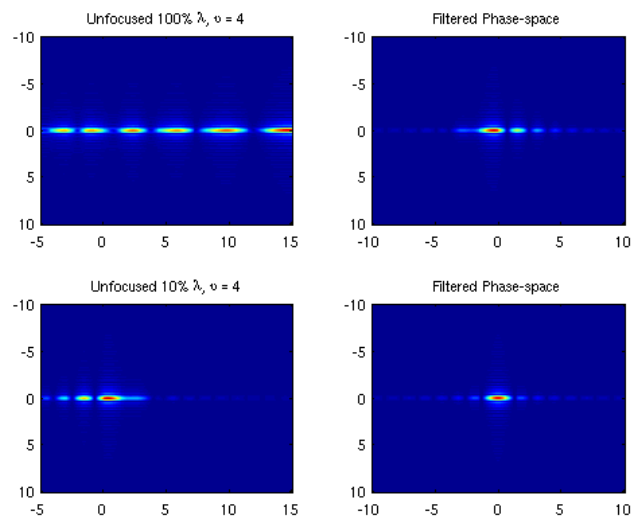


Figure 3.5 : Phase-space focusing with previous filtering

Appendix A

Signals

SAR systems transmit a signal that has to be interpreted once it has been scattered back to the receiver. Since travel times between the antenna and the targets are essential for distance calculations, short pulses would be perfect for estimating such times. Unfortunately, not enough power can be delivered in a short pulse, [7]. Longer signals can deliver higher power. The most commonly used signals in SAR are *linear chirps* [6]. A linear chirp is a signal of the form

$$\begin{aligned} f(t) &= e^{i(-\omega_o t + \sigma t^2)} \chi_{[-\frac{1}{2}, \frac{1}{2}]} \left(\frac{t}{t_c} \right) \\ &= e^{-i\omega_o t} f_B(t), \end{aligned} \quad (\text{A.1})$$

where $\chi_{[-\frac{1}{2}, \frac{1}{2}]}$ is the characteristic function of $[-\frac{1}{2}, \frac{1}{2}]$, and t_c determines the support of the function, and $f_B(t)$ is called *base-band waveform* for a bandwidth B . The frequency modulation parameter is σ and it should be strictly positive. In the frequency domain, the signal has the form

$$\begin{aligned} \hat{f}(\omega) &= \hat{f}_B(\omega - \omega_o) = \int_{-\infty}^{\infty} e^{i(\omega - \omega_o)t + i\sigma t^2} \chi_{[-\frac{1}{2}, \frac{1}{2}]} \left(\frac{t}{t_c} \right) dt \\ &= e^{-\frac{i(\omega - \omega_o)^2}{4\sigma}} \int_{-\infty}^{\infty} \hat{\chi}(w) e^{i\frac{w(\omega - \omega_o)}{2\sigma t_c}} \int_{-\infty}^{\infty} e^{i\sigma(t + \frac{\omega - \omega_o}{2\sigma})^2 - i\frac{w}{t_c}(t + \frac{\omega - \omega_o}{2\sigma})} dt dw \\ &= \sqrt{\frac{i\pi}{\sigma}} e^{-\frac{i(\omega - \omega_o)^2}{4\sigma}} \int_{-\infty}^{\infty} \frac{\hat{\chi}(w)}{2\pi} e^{i\frac{w(\omega - \omega_o)}{2\sigma t_c} - i\frac{w^2}{4\sigma t_c^2}} dw. \end{aligned} \quad (\text{A.2})$$

By taking

$$t_c = \frac{\pi B}{\sigma} \gg \frac{1}{\sqrt{\sigma}} \quad (\text{A.3})$$

then the quadratic term in w in equation (A.2) can be neglected and hence

$$\hat{f}(\omega) = \hat{f}_B(\omega - \omega_o) \approx \sqrt{\frac{i\pi}{\sigma}} e^{-\frac{i(\omega - \omega_o)^2}{4\sigma}} \chi_{[-\frac{1}{2}, \frac{1}{2}]} \left(\frac{\omega - \omega_o}{2\pi B} \right). \quad (\text{A.4})$$

Hence, $\widehat{f}(\omega)$ is supported for the frequencies in

$$|\nu - \nu_o| = \frac{|\omega - \omega_o|}{2\pi} \leq B \quad (\text{A.5})$$

with $\nu_o = \omega_o/(2\pi)$, the carrier frequency. Additionally, the support of the signal should never exceed the repetition time which restricts σ to satisfy $\pi B/\sigma < \Delta s$.

An example of a chirp is portrayed in Figure A.1(a). To time compress the chirps, they are *matched-filtered*. Match-filtering corresponds to convolving the incoming signal with the time-reversed complex conjugate of the transmitted signal. Formally expressed,

$$\mathcal{M}[f](t) = \int f(t' + t) \overline{f(t')} dt', \quad (\text{A.6})$$

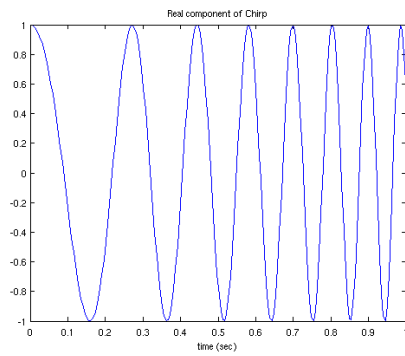
where \overline{f} denotes the complex conjugate of f . By taking the Fourier transform of the match-filtered signal

$$\begin{aligned} \widehat{\mathcal{M}}[f](\omega) &= \int \mathcal{M}[f](t) e^{i\omega t} dt = \widehat{f}(\omega) \overline{\widehat{f}(\omega)} \chi_{[-\frac{1}{2}, \frac{1}{2}]} \left(\frac{\omega - \omega_o}{2\pi B} \right) \\ &= \left| \widehat{f}(\omega) \right|^2 \chi_{[-\frac{1}{2}, \frac{1}{2}]} \left(\frac{\omega - \omega_o}{2\pi B} \right) = \left| \widehat{f}_B(\omega - \omega_o) \right|^2 \chi_{[-\frac{1}{2}, \frac{1}{2}]} \left(\frac{\omega - \omega_o}{2\pi B} \right) \\ &\approx \frac{\pi}{6} \left| \chi_{[-\frac{1}{2}, \frac{1}{2}]} \left(\frac{\omega - \omega_o}{2\pi B} \right) \right|. \end{aligned} \quad (\text{A.7})$$

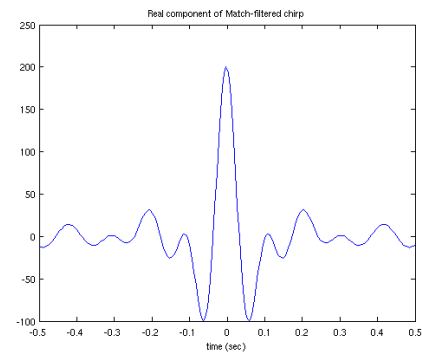
Since $\left| \widehat{f}_B(\omega - \omega_o) \right|^2 \approx \frac{\pi}{6}$ for $\omega \in [\omega_o - \pi B, \omega_o + \pi B]$, then $\left| \widehat{f}_B(\omega - \omega_o) \right|^2 \approx \left| \widehat{f}_B(0) \right|^2$. Therefore,

$$\widehat{\mathcal{M}}[f](\omega) \approx \left| \widehat{f}_B(0) \right|^2, \quad (\text{A.8})$$

for $\omega \in [\omega_o - \pi B, \omega_o + \pi B]$, which is approximately the Fourier transform of a sinc function. The compressed signal has now a support of $O(1/B)$ which is much smaller than t_c . Figure A.1(b) portrays the matched-filtered version of the chirp used in Figure A.1(a). As it can be seen, the pulse is heavily concentrated around $t = 0$.



(a) Linear Chirp signal for $\sigma = 120$,
 $\omega_o = 15$ and $t_c = 2$



(b) Matched-filtered chirp
resembling a sinc function

Figure A.1 : Chirps as Linearly Frequency Modulated waveforms

Appendix B

Modeling of the data

The data acquired by a SAR systems consists of the recorded echoes from the signal that scatter back from the scene to the antenna on the plane. In this appendix, a model for the data will be presented.

Since radar systems use electromagnetic waves, Maxwell's equations are used to describe their behavior, however, in non scattering media each Cartesian component of the waves can be modeled by the scalar wave equation [7].

$$\Delta p(t, \vec{\mathbf{x}}) - \frac{1}{c^2(t, \vec{\mathbf{x}})} \frac{\partial^2 p(t, \vec{\mathbf{x}})}{\partial t^2} = -f(t) \delta(\vec{\mathbf{x}} - \vec{\mathbf{r}}_p(s)) \quad (\text{B.1})$$

where $f(t)$ denotes the transmitted signal from the point-like antenna at position $\vec{\mathbf{r}}_p(s)$ and c is the wave speed. For a homogeneous medium, like air, it satisfies

$$\frac{1}{c^2(t, \vec{\mathbf{x}})} = \frac{1}{c_o^2} [1 - \mathcal{R}(t, \vec{\mathbf{x}})] \quad (\text{B.2})$$

where c_o is the wave speed in air and $\mathcal{R}(t, \vec{\mathbf{x}})$ is the reflectivity.

The solution of equation (B.1) can be decomposed into the scattered and incident fields,

$$p = p_{sc} + p_{in}.$$

The incident field corresponds to the waves as they would travel though a homogeneous medium and the scattered field is the effect of all scatterers in their path. The scattered field can be characterized by the *Lippmann-Schwinger* integral equation [7].

$$p_{sc}(t, \vec{\mathbf{r}}) = \iint G(t - \tau, \vec{\mathbf{r}} - \vec{\mathbf{x}}) \mathcal{R}(\tau, \vec{\mathbf{x}}) \frac{\partial^2 p(\tau, \vec{\mathbf{x}})}{\partial \tau^2} d\tau d\vec{\mathbf{x}} \quad (\text{B.3})$$

where $G(t, \vec{\mathbf{x}}) = \frac{\delta(t - |\vec{\mathbf{x}}|/c_o)}{4\pi|\vec{\mathbf{x}}|}$ is the causal Green's function of the wave equation in homogeneous media.

The scattered waves are commonly approximated by means of the *Born Approximation*, by substituting p_{in} for p in equation (B.3). Hence,

$$p_{sc}(t, \vec{\mathbf{r}}) \approx \iint G(t - \tau, \vec{\mathbf{r}} - \vec{\mathbf{x}}) \mathcal{R}(\tau, \vec{\mathbf{x}}) \frac{\partial^2 p_{in}(\tau, \vec{\mathbf{x}})}{\partial \tau^2} d\tau d\vec{\mathbf{x}}. \quad (\text{B.4})$$

This approximation is used when the reflectivity is either small or it has small support. An in-depth study of the Born approximation in the one-dimensional case is found in [18], where a bound is derived for the difference between the true solution and the approximation. For a more general discussion of the use and validity of the approximation the reader should also see [23], since it is unknown how good this approximations is in more general settings. For the purposes of this thesis, the approximation will be assumed to be valid.

Since the interest lies only in the scattered field its sub-indexing in expression (B.4) will be dropped henceforth and $p_{in}(t, \vec{\mathbf{x}}) = \frac{f(t-|\vec{\mathbf{x}}-\vec{\mathbf{r}}_p(s)|)}{|\vec{\mathbf{x}}-\vec{\mathbf{r}}_p(s)|}$

In the frequency domain, expression (B.4) can be written as

$$\begin{aligned} \widehat{p}(\omega, \vec{\mathbf{r}}) &= \int p(t, \vec{\mathbf{r}}) e^{i\omega t} dt \\ &\approx -\frac{1}{c_o^2} \int \frac{e^{ik|\vec{\mathbf{x}}-\vec{\mathbf{r}}|}}{4\pi|\vec{\mathbf{x}}-\vec{\mathbf{r}}|} \left[\left(\omega_o^2 \widehat{f}(\omega) \frac{e^{ik|\vec{\mathbf{x}}-\vec{\mathbf{r}}_p(s)|}}{4\pi|\vec{\mathbf{x}}-\vec{\mathbf{r}}_p|} \right) * \widehat{\mathcal{R}}(\omega, \vec{\mathbf{x}}) \right] d\vec{\mathbf{x}} \\ &\approx -\frac{\omega_o^2}{c_o^2} \iint \widehat{G}(\omega, \vec{\mathbf{x}}-\vec{\mathbf{r}}) \widehat{G}(\omega-\xi, \vec{\mathbf{x}}-\vec{\mathbf{r}}_p(s)) \times \\ &\quad \widehat{f}(\omega-\xi) \widehat{\mathcal{R}}(\xi, \vec{\mathbf{x}}) d\xi d\vec{\mathbf{x}}. \end{aligned} \quad (\text{B.5})$$

where $\widehat{G}(\omega, \vec{\mathbf{z}}) = \frac{e^{ik|\vec{\mathbf{z}}|}}{4\pi|\vec{\mathbf{z}}|}$, $k = \frac{\omega}{c_o}$, $\widehat{\mathcal{R}}(\xi, \vec{\mathbf{x}}) = \int \mathcal{R}(\tau, \vec{\mathbf{x}}) e^{i\omega\tau} d\tau$, and $*$ denotes a convolution in frequency,

$$\left(\widehat{f}(\omega) \widehat{G}(\omega, \vec{\mathbf{z}}) \right) * \widehat{\mathcal{R}}(\omega, \vec{\mathbf{x}}) = \int \widehat{G}(-xi, \vec{\mathbf{z}}) \widehat{f}(\xi) \widehat{\mathcal{R}}(\omega-\xi, \vec{\mathbf{x}}) d\xi. \quad (\text{B.6})$$

Now the forward model can be defined as an operator \mathfrak{F} acting on reflectivities $\mathcal{R}(t, \vec{\mathbf{x}})$ and mapping them to measurements of the pressure field p at $\vec{\mathbf{r}}_p$.

$$\begin{aligned} \mathfrak{F}[\mathcal{R}](t, \vec{\mathbf{r}}_p(s+t)) &:= \\ &\int \frac{\omega_o^2 f''(t-2|\vec{\mathbf{r}}_p(s+t)-\vec{\mathbf{x}}|/c_o)}{(4\pi c_o |\vec{\mathbf{r}}_p(s+t)-\vec{\mathbf{x}}|)^2} \mathcal{R}(t-|\vec{\mathbf{r}}_p(s+t)-\vec{\mathbf{x}}|/c_o, \vec{\mathbf{x}}) d\vec{\mathbf{x}}. \end{aligned} \quad (\text{B.7})$$

If the scene consist of a stationary point-like target, i.e. $\mathcal{R}(t, \mathbf{x}) = \delta(\vec{\mathbf{x}} - \vec{\rho})$ then

$$\mathfrak{F}[\mathcal{R}](t, \vec{\mathbf{r}}_p(s+t)) = \frac{\omega_o^2 f''(t-2|\vec{\mathbf{r}}_p(s+t)-\vec{\rho}|/c_o)}{(4\pi c_o |\vec{\mathbf{r}}_p(s+t)-\vec{\rho}|)^2}. \quad (\text{B.8})$$

Appendix C

Gotcha

As one of the many spotlight SAR systems available, GOTCHA is X-band persistent surveillance system. In this regime, the aircraft flies a circular path and aims the antenna at a target located within the projection of the circle on the imaging surface.

The desired circular flightpath is assumed to be at height $H = 7.3km$ with radius $R = 7.1km$. The plane will be traveling at a constant speed of $V = 250km/h$ (equivalent to $70m/s$). Targets will usually be at distance $L = 10km$ away from the antenna platform.

For the GOTCHA system considered, the central frequency is $\nu_0 = 9.6GHz$, and hence the central wavelength is $\lambda_o = 3cm$. The bandwidth is $B = 622MHz$ with a sampling of 424 frequencies rendering $\Delta\nu = 1.5MHz$. The signal repetition time is $\Delta s = 0.015s$, which means that a pulse is sent every $1.05m$. The expected resolution for the case of known movement of targets and flightpath perturbations will be for range $c/B = 48cm$ and for cross-range $\lambda_o L/a = 2.5m$.

With this example in mind, a few different scales can be identified in the setup. The next section is devoted to such identification.

Appendix D

Analysis for Phase-space method

D.1 Single target case

Part of the analysis done in [3], done from a single point-like target, is shown here to motivate the algorithm. The perturbations, $\vec{\mu}(s)$, impact travel times in the following way

$$\frac{2}{c_o} |\vec{r}_p(s) + \vec{\mu}(s) - \vec{\rho}(s)| - \tau(s, \vec{\rho}(s)) = \frac{2}{c_o} \vec{\mu}(s) \cdot \vec{m}(s) + O\left(\frac{|\vec{\mu}(s)|^2}{c_o L}\right). \quad (D.1)$$

The effect the modified travel-times have on the image can be seen from the following approximation, up to a multiplicative constant, (denoted as \sim), of the image, as defined in equation (1.1). Henceforth, the lack of time argument for slow-time dependent variables implies evaluation at the center of the sub aperture.

$$\begin{aligned} \mathcal{I}(\rho^{\mathcal{I}}) &\sim \int_{\omega_o - \pi B}^{\omega_o + \pi B} d\omega \exp\left\{\frac{2i\omega}{c_o} \left(|\vec{r}_p - \vec{\rho}| - |\vec{r}_p - \vec{\rho}^{\mathcal{I}}| + \varphi_0\right)\right\} \\ &\sum_{s_i = -S(a)}^{S(a)} \exp\left\{\frac{2i\omega s_i V}{c_o} \left[\vec{t} \cdot (\vec{m} - \vec{m}^{\mathcal{I}}) + \varphi_1\right] + \right. \\ &\left. \frac{i\omega_o (s_i V)^2}{c_o} \left[\frac{\vec{t}'}{V} \cdot (\vec{m} - \vec{m}^{\mathcal{I}}) + \frac{|\mathbb{P}\vec{t}|^2}{|\vec{r}_p - \vec{\rho}|} - \frac{|\mathbb{P}^{\mathcal{I}}\vec{t}|^2}{|\vec{r}_p - \vec{\rho}^{\mathcal{I}}|} + \varphi_2\right]\right\} \end{aligned} \quad (D.2)$$

with the following phases,

$$\begin{aligned} \varphi_0 &= \vec{m}_* \cdot \vec{\mu}, \\ \varphi_1 &= \vec{m} \cdot \frac{\vec{\mu}'}{V} + \vec{t} \cdot \frac{\mathbb{P}\vec{\mu}}{|\vec{r}_p - \vec{\rho}|}, \\ \varphi_2 &= \frac{\vec{\mu}'' \cdot \vec{m}}{V^2} + \frac{2\left(\vec{t} + \frac{\vec{\mu}'}{V}\right) \cdot \mathbb{P}\vec{\mu}'}{|\vec{r}_p - \vec{\rho}|} \cdot \frac{\mathbb{P}\vec{\mu}'}{V} \end{aligned}$$

and $\vec{\rho}_*^{\mathcal{I}} = (\rho_*^{\mathcal{I}}, 0)$, denotes the image peak, $\vec{m}^{\mathcal{I}} = \left(\vec{r}_p - \vec{\rho}^{\mathcal{I}}\right) / \left|\vec{r}_p - \vec{\rho}^{\mathcal{I}}\right|$ and $\mathbb{P}^{\mathcal{I}} = I - \vec{m}^{\mathcal{I}} \left(\vec{m}^{\mathcal{I}}\right)^{\top}$. From equation (D.2), the image will peak when the Fresnel integral

(here a sum) has its peak and the integral over the bandwidth also peaks, i.e. when

$$\varphi_1 = -\vec{\mathbf{t}} \cdot (\vec{\mathbf{m}} - \vec{\mathbf{m}}_{\mathcal{I}}) \quad \varphi_0 = \left| \vec{\mathbf{r}}_p - \vec{\boldsymbol{\rho}}^{\mathcal{I}} \right| - \left| \vec{\mathbf{r}}_p - \vec{\boldsymbol{\rho}} \right|.$$

The analysis is performed under conservative bounds for the magnitude of the perturbation, $|\vec{\boldsymbol{\mu}}(s)|$, its speed, $|\vec{\boldsymbol{\mu}}'(s)|$, and its acceleration, $|\vec{\boldsymbol{\mu}}''(s)|$ are bounded.

$$\begin{aligned} |\vec{\boldsymbol{\mu}}(s)| &\ll \sqrt{\lambda_o L} \ll a, & S^2 |\vec{\boldsymbol{\mu}}''(s)| &\ll \frac{\lambda_o L}{a} \\ S |\vec{\boldsymbol{\mu}}'(s)| &\ll a, & S^3 |\vec{\boldsymbol{\mu}}'''(s)| &\ll \lambda_o, \end{aligned} \quad (\text{D.3})$$

with $S = a/(2V)$, but the method has been shown to focus the images fairly well even when the bounds are not satisfied completely, particularly the bound on $|\vec{\boldsymbol{\mu}}'''(s)|$ is known to be more flexible. However, for the purposes of this section, these bounds will be assumed to be satisfied.

The effect the phases in equation (D.2) have on the focus of the image is seen by linearizing about the true target location. The image peak will be shifted in range and in cross-range respectively by

$$\left| \vec{\mathbf{m}} \cdot (\vec{\boldsymbol{\rho}} - \vec{\boldsymbol{\rho}}_{\star}^{\mathcal{I}}) \right| = O(\varphi_0) \lesssim O\left(\frac{c_o}{B}\right), \quad (\text{D.4})$$

$$\left| \vec{\mathbf{t}} \cdot \frac{\mathbb{P}_{\star}(\vec{\boldsymbol{\rho}} - \vec{\boldsymbol{\rho}}_{\star}^{\mathcal{I}})}{|\vec{\mathbf{r}}_p - \vec{\boldsymbol{\rho}}|} \right| = O(\varphi_1) \sim \frac{\lambda_o L}{a^2} \quad (\text{D.5})$$

Therefore the peak shift in range (equation (D.5)) is small, i.e. compared to the range-resolution, but the shift in cross-range (equation (D.4)) can be large, with respect to cross-range resolution. Additionally, since φ_2 appears in the quadratic part of the phase in the Fresnel integral in equation (D.2), then it only affects the spread of the image in cross-range [3]. Since the quadratic part of the phase also depends on the shift $\vec{\boldsymbol{\rho}} - \vec{\boldsymbol{\rho}}_{\star}^{\mathcal{I}}$, the larger the shift, the more blur in the image.

D.2 Phase estimation

To focus the image, then, these phases need to be estimated and compensated. Much of the analysis in [3] is devoted to careful derivation of conditions when peaks of the Wigner transform and the ambiguity functions can be used to approximate the perturbation. The Wigner transform of the forward model in equation (B.8), evaluated at $\omega = \omega_0$, takes the form

$$\mathbb{W}(s=0, \Omega, \omega_o, T) \sim \frac{\left| \widehat{f}_B(0) \right|^4}{|\vec{\mathbf{r}}_p - \vec{\boldsymbol{\rho}}|^4} \text{sinc}(\pi B [T + \delta T^W]) \text{sinc}\left(\frac{4\pi a c_o (\Omega + \delta \Omega^W)}{2\lambda_o V \omega_o}\right), \quad (\text{D.6})$$

where

$$\delta T^W = \frac{2\vec{\mu} \cdot \vec{\mathbf{m}}}{c_o}, \quad \frac{c_o \delta \Omega^W}{2V\omega_o} = \vec{\mathbf{m}} \cdot \frac{\vec{\mu}'}{V} + \vec{\mathbf{t}} \cdot \frac{\mathbb{P}\vec{\mu}}{|\vec{\mathbf{r}}_p - \vec{\rho}|} \quad (\text{D.7})$$

The peak of this function occurs when both arguments inside the sinc functions are zero. Let (Ω^W, T^W) denote the location of such a peak. Hence the phases that can be approximated so far are,

$$\varphi_0(s) = -\frac{c_o}{2} T^W(s) + O\left(\frac{c_o}{B}\right), \quad \varphi_1(s) = -\frac{\lambda_o}{4\pi V} \Omega^W(s) + O\left(\frac{\lambda_o}{a}\right) \quad (\text{D.8})$$

Similarly, for the ambiguity function for $\tilde{s} = a/(2V)$ can be approximated as follows

$$\mathbb{A}\left(s = 0, \Omega, \frac{a}{2V}, T\right) \sim \frac{|\widehat{f}_B(0)|^4 e^{-i\omega_o \delta T^A}}{|\vec{\mathbf{r}}_p - \vec{\rho}|^4} \text{sinc}(\pi B [T + \delta T^A]) \text{sinc}\left(\frac{a(\Omega + \delta \Omega^A)}{2V}\right) \quad (\text{D.9})$$

where

$$\delta T^A = -\frac{a}{V} \frac{\delta \Omega^W}{\omega_o}, \quad \frac{\delta \Omega^A}{\omega_o} = \frac{Va}{c_o} \left[\frac{2\vec{\mathbf{t}}}{|\vec{\mathbf{r}}_p - \vec{\rho}|} \cdot \frac{\mathbb{P}\vec{\mu}'}{V} + \frac{\vec{\mu}''}{V^2} \cdot \vec{\mathbf{m}} \right]. \quad (\text{D.10})$$

This function will peak at (Ω^A, T^A) , and using these values, the following estimates can be made,

$$\varphi_1(s) = \frac{c_o}{2a} T^A(s) + O\left(\frac{c_o}{aB}\right), \quad \varphi_2(s) = -\frac{\lambda_o}{2\pi aV} \Omega^A(s) + O\left(\frac{\lambda_o}{a^2}\right). \quad (\text{D.11})$$

Since $\lambda_o/a \ll c_o/(aB)$, then the new estimate for φ_1 coming from the ambiguity function should not be used since it has lower resolution. Hence, the estimation of the perturbations is given by

$$\vec{\mu}^{PS}(s) = \left[\varphi_0 + sV\varphi_1 + \frac{(sV)^2}{2}\varphi_2 \right] \vec{\mathbf{m}}(s) \quad (\text{D.12})$$

Bibliography

- [1] R. Bamler. A comparison of range-doppler and wavenumber domain sar focusing algorithms. *Geoscience and Remote Sensing, IEEE Transactions on*, 30(4):706 –713, jul 1992.
- [2] S. Barbarossa and A. Farina. A novel procedure for detecting and focusing moving objects with sar based on the wigner-ville distribution. In *Radar Conference, 1990., Record of the IEEE 1990 International*, pages 44 –50, may 1990.
- [3] L Borcea, T Callaghan, and G Papanicolaou. Synthetic aperture radar imaging with motion estimation and autofocus. *Inverse Problems*, 28(4):045006, 2012.
- [4] W.G. Carrara, R.S. Goodman, and R.M. Majewski. *Spotlight Synthetic Aperture Radar: Signal Processing Algorithms*. The Artech House Remote Sensing Library. Artech House, 1995.
- [5] Jr. Charles V. Jakowatz and Daniel E. Wahl. Eigenvector method for maximum-likelihood estimation of phase errors in synthetic-aperture-radar imagery. *J. Opt. Soc. Am. A*, 10(12):2539–2546, Dec 1993.
- [6] E Chassande-Mottin and P Flandrin. On the timefrequency detection of chirps. *Applied and Computational Harmonic Analysis* 6, 1999.
- [7] M Cheney and B Borden. *Fundamentals of Radar Imaging*. CBMS-NSF Regional Conference Series in Applied Mathematics. Society for Industrial Mathematics, 2009.
- [8] J Curlander and R McDonough. *Synthetic Aperture Radar*. Wiley Series in Remote Sensing. Wiley Interscience, 1991.
- [9] L J Cutrona, W E Vivian, E N Leith, and G O Hall. A high-resolution radar combat-surveillance system. *IRE Transactions on Military Electornics*, 1961.
- [10] Yu Ding and David C. Munson. Time-frequency methods in sar imaging of moving targets. In *Acoustics, Speech, and Signal Processing (ICASSP), 2002 IEEE International Conference on*, volume 3, pages III–2881 –III–2884, may 2002.

- [11] Yu Ding, Ning Xue, and Jr. Munson, D.C. An analysis of time-frequency methods in sar imaging of moving targets. In *Sensor Array and Multichannel Signal Processing Workshop. 2000. Proceedings of the 2000 IEEE*, pages 221–225, 2000.
- [12] P Eichel, D Ghiglia, and C Jakowatz. A new phase correction method for synthetic aperture radar. *Proceedings of the Digital Signal Processing Workshop at Stanford Sierra Lodge*, 1988.
- [13] P Eichel, D Ghiglia, and C Jakowatz. Speckle processing method for synthetic-aperture-radar phase correction. *Opticas Letters*, 1989.
- [14] P.H. Eichel, D.C. Ghiglia, C.V. Jakowatz, and D.E. Wahl. Phase gradient autofocus for sar phase correction: Explanation and demonstration of algorithmic steps. In *Digital Signal Processing workshop, 1992. The*, pages 6.6.1 –6.6.2, sep 1992.
- [15] G. Franceschetti and G. Schirinzi. A sar processor based on two-dimensional fft codes. *Aerospace and Electronic Systems, IEEE Transactions on*, 26(2):356–366, mar 1990.
- [16] T. J. Kragh. Monotonic iterative algorithm for minimum-entropy autofocus. In *Adaptive Sensor Array Processing (ASAP) Workshop*, 2006.
- [17] M. Kuźniak and M. Malanowski. Implementation of phase gradient autofocus algorithm for spotlight SAR. In *Society of Photo-Optical Instrumentation Engineers (SPIE) Conference Series*, volume 6937 of *Presented at the Society of Photo-Optical Instrumentation Engineers (SPIE) Conference*, January 2008.
- [18] R M Lewis and W W Symes. On the relation between the velocity coefficient and boundary value for solutions of the one-dimensional wave equation. *Inverse Problems*, 7(4):597, 1991.
- [19] Aining Li and O. Loffeld. Two dimensional sar processing in the frequency domain. In *Geoscience and Remote Sensing Symposium, 1991. IGARSS '91. Remote Sensing: Global Monitoring for Earth Management., International*, volume 2, pages 1065 –1068, jun 1991.
- [20] R.L. Morrison and Minh N. Do. Multichannel autofocus algorithm for synthetic aperture radar. In *Image Processing, 2006 IEEE International Conference on*, pages 2341 –2344, oct. 2006.
- [21] Robert L. Morrison and Minh N. Do. A multichannel approach to metric-based sar autofocus. In *in Proc. of the IEEE International Conference on Image Processing*, pages 1070–1073, 2005.

- [22] Claude E. Shannon. A mathematical theory of communication. *The Bell system technical journal*, 27:379–423, July 1948.
- [23] William Symes. *Mathematics of reflection seismology*, 1995.
- [24] A. F. Yegulap. Minimum entropy sar autofocus. In *Proceedings, Adaptive Sensor Array Processing (ASAP) Workshop.*, 1999.
- [25] Q Zhang, T S Yeo, G Du, and S Zhang. Estimation of three-dimensional motion parameters in interferometric isar imaging. *IEEE Transactions on GeoScience and Remote Sensing*, 2004.